

STRUCTURED RED GIANT WINDS WITH MAGNETIZED HOT BUBBLES AND THE CORONA/COOL WIND DIVIDING LINE

TAKERU K. SUZUKI¹

Submitted to ApJ

ABSTRACT

By performing magnetohydrodynamical (MHD) simulations, we investigate mass loss of intermediate- and low-mass stars from main sequence to red giant branch phases. Alfvén waves, which are excited by the photospheric perturbations due to the surface convections, travel outwardly and dissipate by nonlinear processes to accelerate and heat stellar winds. We dynamically treat these processes in open magnetic field regions from the photospheres to $\simeq 25$ stellar radii. An advantage of our simulations is that the physical conditions of winds, such as mass loss rates, \dot{M} , outflow velocities, and temperatures, are determined from the properties of the surface convections in a self-consistent manner. When the star evolves to slightly blueward positions of the dividing line (Linsky & Haisch), the steady hot corona with temperature, $T \approx 10^6$ K, suddenly disappears. Instead, many hot ($\sim 10^6$ K) and warm ($\gtrsim 10^5$ K) bubbles are formed in cool ($T \lesssim 2 \times 10^4$ K) chromospheric winds because of thermal instability; the RGB star wind is not a steady stream but structured outflow. These bubbles are created favorably in fast MHD shock structures and supported by magnetic pressure. The densities of the bubbles can be kept low to reduce the radiative cooling so that the bubbles survive rather long time. Even in the stars redward of the dividing line, hot bubbles intermittently exist, and they can be sources of ultraviolet/soft X-ray emissions from hybrid stars. \dot{M} of RGB stars largely vary in time because of many bubbles and blobs; for example \dot{M} of a simulated $3M_{\odot}$ star with surface gravity, $\log g = 1.4$, varies from 1×10^{-10} to $5 \times 10^{-7} M_{\odot} \text{ yr}^{-1}$. Along with the stellar evolution, the wind velocity also rapidly decreases to \lesssim several 10 km s^{-1} which is considerably slower than the escape velocity at the stellar surface. This is because an “effective surface” is formed at several stellar radii below which the time-averaged atmosphere is almost static. The acceleration of the wind starts from there, hence, the wind speed is regulated by the slower escape velocity at that location.

Subject headings: magnetic fields – stars: coronae – stars: late type – stars: mass loss – stars: winds, outflows – waves

1. INTRODUCTION

Solar-type stars have X-ray emitting coronae with temperatures, $T \gtrsim 10^6$ K, and hot stellar winds stream out with asymptotic terminal velocities, $v_{\infty} = 100 - 1000 \text{ km s}^{-1}$, comparable to the escape velocities at the surfaces. The total masses lost by the winds are negligible during the main sequence (MS) phase in comparison with the stellar masses, whereas the winds may play a role in the loss of the angular momentums. As solar-type stars evolve to red giant branch (RGB), the mass loss rates, \dot{M} , increase by 4-10 orders of magnitude (Judge & Stencel 1991), while v_{∞} drop to $10 - 100 \text{ km s}^{-1}$, smaller than the surface escape velocities. In addition, the temperatures of the winds also decrease, which is probably drastic around the “dividing line” (DL hereafter; Linsky & Haisch 1979) discussed below. The mass loss during the RGB phase becomes more important, and it may control the later evolution of the star. For instance, it is inferred that the formation of blue horizontal branch stars is related to the mass losses during RGB phase (Yi, Demarque, & Kim 1997). In spite of its importance, however, the acceleration mechanism of RGB star winds is not well understood.

It was reported that cool single RGB stars redward of the DL near spectral type K1 III in Hertzsprung-

Russel (HR)-diagram (Figure 1) showed an evidence of neither ultraviolet (UV) radiation of C_{IV} ($T \sim 10^5$ K) (Linsky & Haisch 1979) nor soft X-ray ($T \sim 10^6$ K) (Ayres et al. 1981). Stencel & Mullan (1980) further pointed out that the stellar winds appear cool and massive after stars cross the DL.

However, Hartmann, Dupree, & Raymond (1980) observed late-type super-giants in the noncoronal zone which exhibit both UV emission and blue-shifted chromospheric absorption features, indicating that hot gas and cool outflow coexist. Such hybrid stars were also detected in the noncoronal zone by later observations (e.g. Ayres et al. 1998), whereas the activity levels of UV/soft X-ray are much lower than in the coronal zone. These things show that the simple DL picture roughly holds while the reality seems a bit more complicated.

RGB stars are generally slow rotators. The radiation luminosities of intermediate- and low-mass stars near the DL are not still large, either. Therefore, the centrifugal force and radiation pressure are not sufficient in accelerating the stellar winds (e.g. Judge & Stencel 1991). Instead, the surface convective layer is expected to be the main origin of driving the winds and UV/X-ray activities. Magnetic fields are probably generated by turbulent dynamo in the convection zone. The energy of the surface turbulences is lifted up through the magnetic fields, and the dissipation of the energy in upper regions leads to the heating of the atmosphere and the acceler-

Electronic address: stakeru@provence.c.u-tokyo.ac.jp

¹ Graduate School of Arts and Sciences, University of Tokyo, Komaba, Meguro, Tokyo, Japan 153-8902

ation of the wind. This picture is essentially the same as what takes place in the solar corona and wind. Difference from the sun is that the surface gravity is much smaller in RGB stars. In a naïve way of thinking, the transition from the steady coronae to the cool winds (with some hybrid activities) is possibly explained by this gravity effect even though other conditions are similar; due to insufficient confinement by the gravity, cool atmosphere flows out before heated up to coronal temperature ($T \sim 10^6$ K).

Many pioneering works have tried to reveal nature of RGB star winds (e.g. Hartmann & MacGregor 1980; Holzer, Flå, & Leer 1983; Charbonneau & MacGregor 1995). However, the consecutive processes from the surface to the wind explained above have not been studied self-consistently; previous model calculations started from locations far above the photosphere in order to avoid difficulties arising from the huge density contrast. Moreover, they assume mechanical or phenomenological “wave” energies with somewhat ad hoc prescription of the dissipation.

In this paper, we perform dynamical simulations of stellar winds from the photosphere to $\simeq 25 R_\star$ in open magnetic field regions, where R_\star is stellar radius. We give perturbations at the photosphere originating from the surface convection. These fluctuations excite waves which propagate upwardly. Among various modes the Alfvén wave travel to a sufficiently large distance to contribute to the acceleration and heating of the stellar wind. We simulate the propagation and dissipation of waves by solving the nonlinear MHD equations, and treat the heating and acceleration of the gas in a fully self-consistent manner without conventional heating functions often adopted in previous calculations (§3.6). The wind properties, such as \dot{M} and v_∞ , are determined from the surface conditions without ad hoc parameters. Another advantage of dynamical simulations is that we do not have to care about the critical (sonic) point(s) which is often problematic when constructing a transonic wind solution under the steady-state condition. A stable wind structure is automatically selected whether it is transonic or subsonic.

We carried out simulations in the solar corona and wind (Suzuki & Inutsuka 2005, 2006). We showed that the coronal heating and solar wind acceleration in the open field regions are natural consequences of the photospheric perturbations; Alfvén waves generated from the surface effectively dissipate in the corona by nonlinear mechanism to sufficiently heat and accelerate the solar wind in spite of the energy loss via radiative cooling, thermal conduction, and wave reflection. The aim of this paper is to study evolution of stellar winds from MS to RGB stages by extending our solar work to cool RGB stars. We investigate stellar winds of $1 M_\odot$ star from MS (*i.e.* present sun) to RGB across the DL, where M_\odot is the solar mass. For comparison we also study more massive RGB stars with $3 M_\odot$ both blueward and redward of the DL.

In §2 we describe our simulation method. In §3 we focus on change of the wind properties with the stellar evolution by using the time-averaged structures of the simulated stellar winds. In §4 we investigate the time-dependent wind structures of the RGB stars near the DL.

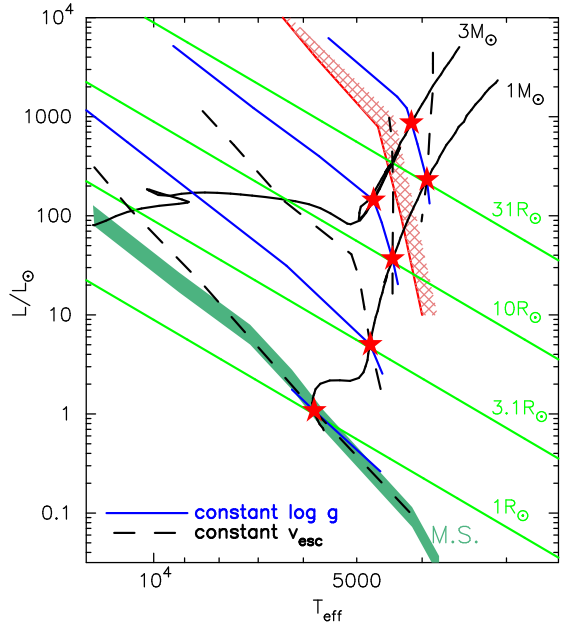


FIG. 1.— Simulated stars in HR-diagram. The six red stars correspond to Models tabulated in Table 1. The black solid lines are the evolutionary paths of $1 M_\odot$ and $3 M_\odot$ stars (Girardi et al. 2000). The red line with the cross hach is the DL (Linsky & Haisch 1979). The green solid lines indicate constant stellar radii, $R_\star = 1 R_\odot$, $3.1 R_\odot$, $10 R_\odot$, and $31 R_\odot$ from the below. The blue lines indicate constant gravity, $\log g = 4.4$, 3.4 , 2.4 , 1.4 from the below. The black dashed lines indicate constant escape speeds from the stellar surfaces, $v_{\text{esc},0} = 617$, 347 , 195 , 110 km s $^{-1}$ from the below. The dark green shaded region denotes the location of main sequence stars.

We discuss comparisons with related works as well as the uncertainties and limitations of our simulations in §5.

2. SIMULATION SET-UP

2.1. Simulated Stars

We simulate the Alfvén wave-driven stellar winds of the various stars summarized in Table 1 and in Figure 1. First, we consider $1 M_\odot$ stars with different $R_\star = 1 R_\odot$ (*i.e.* the present sun), $3.1 R_\odot$, $10 R_\odot$, and $31 R_\odot$, where R_\odot is solar radius, to study the evolution of the winds; note that the DL is between the latter two cases. We also simulate stars with $3 M_\odot$ near the DL to compare with the $1 M_\odot$ cases. Here we adopt the stellar evolutionary tracks from Girardi et al. (2000) to determine the basic stellar parameters, such as R_\star and effective temperatures, T_{eff} , for given stellar mass, M_\star , which are used to estimate the densities at the photospheres, ρ_0 , and the photospheric amplitudes, δv_0 , of the surface convection (§2.3).

2.2. Simulation Details

We consider 1D flux tubes which are super-radially open. As shown in Figure 2, a certain fraction of the stellar surface is covered by closed loop structures so that open flux tubes diverge more rapidly than the radial expansion (Kopp & Holzer 1976).

We inject velocity and magnetic field fluctuations originating the surface convection at the photospheres which are the inner boundaries of the simulations (§2.3). These fluctuations excite various waves which propagate upwardly. We treat both energy and momentum transfers

Model	$M_*(M_\odot)$	$R_*(R_\odot)$	$T_{\text{eff}}(\text{K})$	$\log g$	$v_{\text{esc},0}(\text{km s}^{-1})$	$\rho_0(\text{g cm}^{-3})$	$\langle \delta v_0 \rangle(\text{km s}^{-1})$	$\tau_{\text{min}}(\text{min})$	$\tau_{\text{max}}(\text{min})$	$R_1(R_*)$	$R_2(R_*)$
I	1	1	5900	4.4	617	10^{-7}	1.0	1	32	1.01	1.2
II	1	3.1	4800	3.4	347	5×10^{-8}	1.5	9	290	1.031	1.4
III	1	10	4500	2.4	195	1.5×10^{-8}	2.8	87	2800	1.1	1.5
IV	1	31	3900	1.4	110	4.5×10^{-9}	5.3	800	25600	1.31	1.8
V	3	17.3	4700	2.4	255	1.5×10^{-8}	3.7	90	2900	1.1	1.5
VI	3	54.8	4200	1.4	144	4×10^{-9}	8.0	930	29900	1.31	1.8

TABLE 1

MODEL PROPERTIES. TABULATED FROM LEFT TO RIGHT ARE RESPECTIVELY STELLAR MASS, M_* , IN M_\odot , STELLAR RADIUS, R_* , IN R_\odot , EFFECTIVE TEMPERATURE, T_{eff} (K), LOGARITHM OF SURFACE GRAVITY, $g = GM_*/R_*^2$, ESCAPE SPEED AT THE SURFACE, $v_{\text{esc},0} \equiv v_{\text{esc}}(R_*) = \sqrt{2GM_*/R_*}$, PHOTOSPHERIC DENSITY, $\rho_0(\text{g cm}^{-3})$, ROOT-MEAN-SQUARED AMPLITUDE OF TRANSVERSE FLUCTUATION AT THE PHOTOSPHERE, $\langle \delta v_0 \rangle$ (km s $^{-1}$), MINIMUM WAVE PERIOD, τ_{min} , MAXIMUM WAVE PERIOD, τ_{max} , AND LOCATIONS OF FLUX TUBE EXPANSIONS, R_1 AND R_2 .

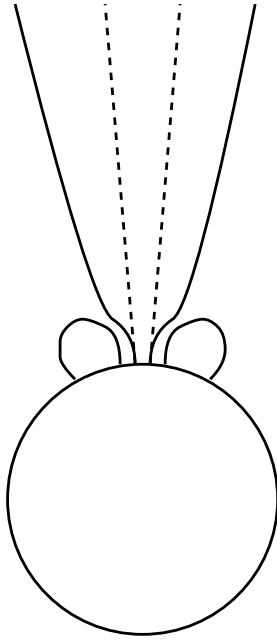


FIG. 2.— Schematic picture of a magnetic flux tube which is super-radially open. The solid lines denote magnetic field lines. The open field region expands more rapidly than the spherical expansion shown by the dashed lines. Our simulations treat such flux tubes which are open super-radially.

in stellar winds, namely the propagation and dissipation of the waves and the consequent acceleration and heating of the surrounding gas, in a self-consistent manner. We set the outer boundaries at $\simeq 25 R_*$ at which the outgoing condition of both materials and MHD waves is properly prescribed (Suzuki & Inutsuka 2006). In this paper we neglect centrifugal force, which is a reasonable assumption since low mass MS stars and RGB stars generally rotate slowly. We also neglect radiation pressure, which is also appropriate, where it might become important in more evolved asymptotic giant branch stars which have dusts in the atmospheres.

Radial field strength, B_r , is given by conservation of magnetic flux as

$$B_r r^2 f(r) = \text{const.}, \quad (1)$$

where $f(r)$ is a super-radial expansion factor. A 1D flux tube is fixed by field strength at the photosphere, $B_{r,0}$, and $f(r)$. We set $B_{r,0}$ and $f(r)$ based on our previous solar studies. While the average field strength is 1–10 G on the solar photosphere, magnetic field lines are

swept into inter-granulation lanes so that the localized strength becomes $\gtrsim 100$ G to a few kG. These field lines rapidly expand and becomes $\lesssim 10$ G in the coronal region. Finally in the outer region (\gtrsim a few R_*) the field lines distribute almost radially.

We use the the same $B_{r,0} = 240$ G and the same total expansion factor, $f_{\text{tot}} = 240$, for all the Models. Note that these values give $B_{r,0}/f_{\text{tot}} = 1$ G which is the total magnetic flux of the open field regions divided by the stellar surface. The average field strength becomes larger by adding the contributions from the closed structures (§5.1). We use the same functional form of the expansion as in Suzuki & Inutsuka (2006; see also Kopp & Holzer 1976):

$$f(r) = \frac{f_{1,\text{tot}} \exp(\frac{r-R_1}{\sigma_1}) + f_1}{\exp(\frac{r-R_1}{\sigma_1}) + 1} \frac{f_{2,\text{tot}} \exp(\frac{r-R_2}{\sigma_2}) + f_2}{\exp(\frac{r-R_2}{\sigma_2}) + 1} \quad (2)$$

where $f_1 = 1 - (f_{1,\text{tot}} - 1) \exp(\frac{R_*-R_1}{\sigma_1})$ and $f_2 = 1 - (f_{2,\text{tot}} - 1) \exp(\frac{R_*-R_2}{\sigma_2})$. The flux tube initially expands by a factor of $f_{1,\text{tot}}$ around $R_1 - \sigma_1 \sim R_1 + \sigma_1$ corresponding to the 'funnel' structure (Tu et al. 2005) by closed loops, and followed by $f_{2,\text{tot}}$ times expansion around $R_2 - \sigma_2 \sim R_1 + \sigma_2$ due to the large scale (dipole) magnetic fields. The total super-radial expansion is defined as $f_{\text{tot}} = f_{1,\text{tot}} f_{2,\text{tot}}$. We adopt $f_{1,\text{tot}} = 40$ and $f_{2,\text{tot}} = 6$ in all the Models. R_1 and R_2 of each Model are summarized in Table 1. $R_1 - R_*$ is set to be (roughly) proportional to the scale height ($\propto g^{-1} = (GM_*/R_*)^{-1}$; see Equation 13 for a more specific form) because closed loops would be taller in lower gravity stars if the surface magnetic field conditions are the same (but see §5.1). Accordingly R_2 is also set to be larger in the evolved stars. We adopt the 'widths' of the expansions, $\sigma_1 \approx 0.6(R_1 - R_*)$ and $\sigma_2 \approx 0.6(R_2 - R_*)$. Actually, the most important parameter which determines the stellar wind structure is f_{tot} and the other parameters, R_1 , R_2 , σ_1 , σ_2 , $f_{1,\text{tot}}$, and $f_{2,\text{tot}}$ only give small corrections.

We dynamically solve ideal MHD equations with radiative cooling and thermal conduction :

$$\frac{d\rho}{dt} + \frac{\rho}{r^2 f} \frac{\partial}{\partial r} (r^2 f v_r) = 0, \quad (3)$$

$$\rho \frac{dv_r}{dt} = -\frac{\partial p}{\partial r} - \frac{1}{8\pi r^2 f} \frac{\partial}{\partial r} (r^2 f B_\perp^2) + \frac{\rho v_\perp^2}{2r^2 f} \frac{\partial}{\partial r} (r^2 f) - \rho \frac{GM_*}{r^2}, \quad (4)$$

$$\rho \frac{d}{dt}(r\sqrt{f}v_{\perp}) = \frac{Br}{4\pi} \frac{\partial}{\partial r}(r\sqrt{f}B_{\perp}). \quad (5)$$

$$\rho \frac{d}{dt} \left(e + \frac{v^2}{2} + \frac{B^2}{8\pi\rho} - \frac{GM_{\star}}{r} \right) + \frac{1}{r^2 f} \frac{\partial}{\partial r} \left[r^2 f \left\{ (p + \frac{B^2}{8\pi})v_r - \frac{Br}{4\pi}(\mathbf{B} \cdot \mathbf{v}) \right\} \right] + \frac{1}{r^2 f} \frac{\partial}{\partial r}(r^2 f F_c) + q_R = 0, \quad (6)$$

$$\frac{\partial B_{\perp}}{\partial t} = \frac{1}{r\sqrt{f}} \frac{\partial}{\partial r}[r\sqrt{f}(v_{\perp}Br - v_r B_{\perp})], \quad (7)$$

where ρ , \mathbf{v} , p , \mathbf{B} are density, velocity, pressure, and magnetic field strength, respectively, and subscript r and \perp denote radial and tangential components; $\frac{d}{dt}$ and $\frac{\partial}{\partial t}$ denote Lagrangian and Eulerian derivatives, respectively; $e = \frac{1}{\gamma-1} \frac{p}{\rho}$ is specific energy and we assume the equation of state for ideal gas with a ratio of specific heat, $\gamma = 5/3$; G is the gravitational constant; $F_c = \kappa_0 T^{5/2} \frac{dT}{dr}$ is thermal conductive flux by Coulomb collisions, where $\kappa_0 \approx 10^{-6}$ in c.g.s unit; q_R is radiative cooling. In this paper we assume the solar elemental abundance for the radiative cooling term. In sufficiently low density regions with $\rho \leq 5 \times 10^{-17}$ g cm $^{-3}$ we use optically thin radiative loss, $q_R = n_p n_e \Lambda$, where n_p and n_e are proton and electron number densities and Λ is the tabulated cooling function by Landini & Monsignori-Fossi (1990). In denser regions, which generally corresponds to chromosphere, we adopt empirical radiative cooling, $q_R = 4.5 \times 10^9 \rho$ (erg cm $^{-3}$ s $^{-1}$) derived from observations of the solar chromosphere (Anderson & Athay 1989; Moriyasu et al. 2004) to take into account the optically thick effect. For simplicity's sake we switch off the cooling if the temperature drops below 3000 K, which sometimes happens in the evolved stars with small $\log g$. We might have to take into account effects of neutral atoms or dusts in such low temperature, though we do not do explicitly in this paper (see §5.4).

We adopt the second-order MHD-Godunov-MOCCT scheme (Sano & Inutsuka 2006; see also Suzuki & Inutsuka 2006) to update the physical quantities. In this scheme each cell boundary is treated as discontinuity, and for the time evolution we solve the nonlinear Riemann shock tube problem with the magnetic pressure term by using the Rankine-Hugoniot relations. Therefore, entropy generation, namely heating, is automatically calculated from the shock jump condition. A great advantage of our code is that no artificial viscosity is required even for strong MHD shocks; numerical diffusion is suppressed to the minimum level for adopted numerical resolution.

2.3. Surface Conditions

We describe the conditions of the stellar photospheres which are the inner boundaries of the simulations. As shown in Table 1, the photospheric density, ρ_0 , is smaller in the more evolved star. This is because pressure, p_0 , at photosphere (defined as optical depth ≈ 1) has a positive dependence on gravity,

$$p_0 \propto g^{0.6}, \quad (8)$$

where $g = GM_{\star}/R_{\star}^2$ (§9 of Gray 1992).

Amplitude, δv_0 , of surface fluctuations can be estimated from convective flux. Generation of sound waves on late-type stars have been extensively studied

(Lighthill 1952; Stein 1967; de Loore 1970; Renzini et al. 1977; Bohn 1984; Shibahashi 2005). Recently, numerical experiments of surface convection are also carried out (Stein et al. 2004). These works show that excited acoustic flux, $F_{a,0}$ (erg cm $^{-2}$ s $^{-1}$), has a negative dependence on surface gravity and a positive dependence on stellar effective temperature. In this paper we adopt the relation derived by Renzini et al. (1977),

$$F_{a,0} \propto g^{-0.7} T_{\text{eff}}^{12}, \quad (9)$$

whereas other works also give similar trends. Acoustic wave flux is the combination of density, longitudinal (radial direction) amplitude, $\delta v_{\parallel,0}$, and sound speed, c_s : $F_{a,0} = \rho \langle \delta v_{\parallel,0}^2 \rangle c_s$, where $\langle \rangle$ denotes time-average. Observations of solar granulations show that both transverse and longitudinal amplitudes are similar, $\langle \delta v_{\parallel,0} \rangle \approx \langle \delta v_{\perp,0} \rangle \approx 1 - 2$ km s $^{-1}$ (Holweger et al. 1978), where $\langle \delta v_{\parallel,0} \rangle = \sqrt{\langle \delta v_{\parallel,0}^2 \rangle}$ and $\langle \delta v_{\perp,0} \rangle = \sqrt{\langle \delta v_{\perp,0}^2 \rangle}$. We assume that this also holds in RGB stars and we simply write $\langle \delta v_0 \rangle$ here. We set $\langle \delta v_0 \rangle = 1.0$ km s $^{-1}$ in the present sun (Model I), and then, $\langle \delta v_0 \rangle$ of the other stars can be estimated from the relation of Equation (9). $\langle \delta v_0 \rangle$'s in Table 1 are derived by this way.

Typical period, τ , of generated waves are also related to stellar parameters. Simulations by Stein et al. (2004) give

$$\tau \propto g^{-1}. \quad (10)$$

This relation can be understood by the following simple argument. τ can be scaled by turn over time of eddies (granulation cells), $\sim l/c_s$, where l is a typical granulation size, if stochastic processes of the convection dominate in the wave generation. l 's of different stars are probably proportional to the pressure scale heights, $H_p \approx c_s^2/g$. Then,

$$\tau \sim l/c_s \propto H_p/c_s \sim c_s/g. \quad (11)$$

The c_s dependence does not appear in Equation (10) because the difference of $c_s(\propto T_{\text{eff}})$ is small in the simulated stars in Stein et al. (2004). We use Equation (11) to give realistic spectra of fluctuations at the photosphere. In this paper, we assume power spectrum of $P(\nu) \propto \nu^{-1}$ with respect to frequency, $\nu = 1/\tau$, where the normalization is given by $\langle \delta v_0^2 \rangle = \int_{\nu_{\text{min}}}^{\nu_{\text{max}}} d\nu P(\nu)$. For the present sun, we set $\tau_{\text{min}} = 1/\nu_{\text{max}} = 1$ min and $\tau_{\text{max}} = 1/\nu_{\text{min}} = 32$ min, giving ≈ 5 min, which dominates the solar oscillations, as the (logarithmic) mean value. For the other Models we set τ_{min} and τ_{max} by using the scaling relation of Equation (11) (Table 1). It should be noted that a shape of $P(\nu)$ affects results of wind structures little as long as the same τ_{min} and τ_{max} are adopted (Suzuki & Inutsuka 2006).

In this paper we only consider the open field regions in which the unperturbed magnetic fields are oriented to the vertical direction at the surfaces. In such a situation, if we restrict waves traveling in the vertical direction, the transverse components of surface fluctuations produce Alfvén waves, while the longitudinal component excites compressive waves, e.g. acoustic waves, or more generally, magnetosonic waves. The uncompressive character enables the Alfvén wave to propagate a long distance. On the other hand, longitudinal waves

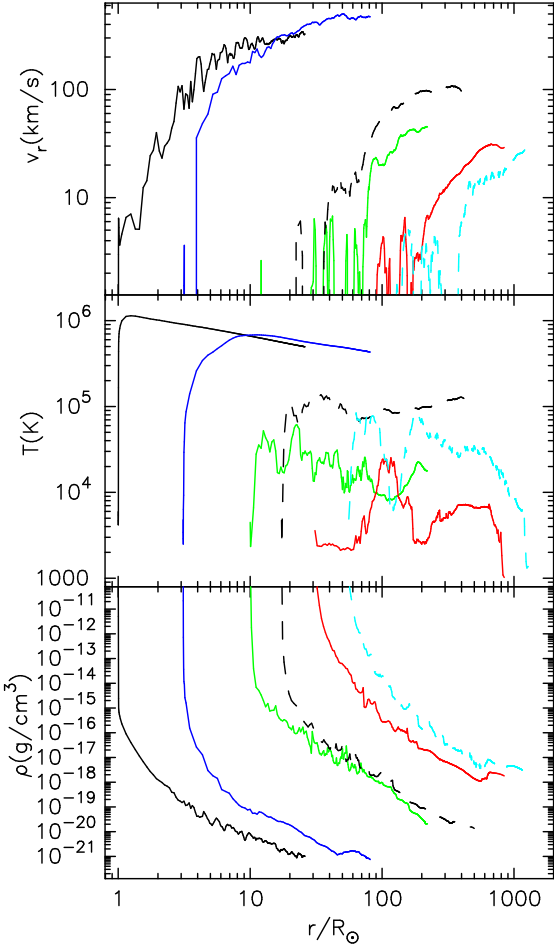


FIG. 3.— Stellar wind structures of the six Models. From the top to the bottom, radial outflow velocity, v_r (km s $^{-1}$), temperature, T (K), and density, ρ (g cm $^{-3}$), are plotted. The solid lines are the results of the $1 M_\odot$ stars; the black, blue, green, and red lines are the results of Models I, II, III, and IV, respectively. The dashed lines are the results of the $3 M_\odot$ stars; the black and light-blue lines are the results of Models V and VI.

are quite dissipative because both nonlinear shock formation (Suzuki 2004) and collisionless dissipation processes (Suzuki et al. 2006) affect propagation of those waves. Thus, compressive waves cannot travel a sufficiently long distance to contribute to the acceleration of winds (Suzuki 2002). Actually, we tested a role of longitudinal fluctuations in several models and found that its effect is limited in the regions near the surface ($\ll 2 R_\star$). Therefore, we only show the results of transverse fluctuations at the photospheres in this paper.

3. EVOLUTION OF STELLAR WINDS —TIME-AVERAGED RESULTS—

We initially set up the static and cool atmospheres with the photospheric temperatures. We start the simulations by injecting the transverse fluctuations from the photospheres which excite Alfvén waves (see the *electronic edition* for the mpeg file of Model VI which is the movie version of Figure 12). The atmospheres are accelerated as transonic winds in all the six Models by the dissipation of the Alfvén waves (§3.6). This shows that the transonic outflow is a stable and natural consequence of the Alfvén wave-driven winds of both MS

and RGB stars. The stellar winds are settled down to quasi-steady states after \gtrsim twice of the sound crossing times of the entire simulation boxes (the sound speeds are slower than the Alfvén speeds in our simulations), although the RGB cases (Models III-VI) show large fluctuations in the winds by thermal instability (§4). In this section we study evolution of stellar winds from MS to RGB by examining the time-averaged wind structures.

3.1. Overall Trends

Figure 3 presents the structures of outflow velocity, v_r (km s $^{-1}$) (top), temperature, T (K) (middle), and density, ρ (g cm $^{-3}$) (bottom) on radial distances from the stellar centers in unit of R_\odot . The quantities are averaged over sufficiently longer durations than τ_{\max} of each Model. One can clearly see the disappearance of the hot corona with the stellar evolution from the sub-giant (SB; Model II) to the RGB (Models III - VI) cases. Coupled with the disappearance of the steady corona, the wind becomes dense and slow.

MS (Model I; the present Sun) as well as SB (Model II) stars possess the hot ($\approx 10^6$ K) coronae and the fast (> 300 km s $^{-1}$ at $20 R_\star$) winds. As the star expands, the temperature rapidly decreases to $10^4 - 10^5$ K. One may point out that Models III and V are still blueward of the DL, hence, the disappearance of the corona is too early. However, hot regions with $10^5 - 10^6$ K, which can be sources of UV/X-ray radiation, are created intermittently in these stars, as will be shown later in the snap-shot results (§4), although they are not observed in the time-averaged structures since they are moving outwardly.

The main reason of the disappearance of the *steady* corona is that the hot plasma cannot be confined by the stellar gravity any more since the sound speed (≈ 150 km s $^{-1}$) of $\sim 10^6$ K plasma exceeds the escape speed, $v_{\text{esc}}(r) = \sqrt{2GM_\star/r}$, at $r \gtrsim$ a few R_\star . Thermal instability is also involved, which leads to the rapid decrease of the temperature (§3.2).

The wind speeds also drop to 10-100 km s $^{-1}$ at $20 R_\star$ in the RGB stars. Although the terminal velocities may be slightly larger when considering the acceleration in $r > 20 R_\star$, they must be considerably smaller than the escape velocities, $v_{\text{esc},0} (\equiv v_{\text{esc}}(R_\star)) = \sqrt{2GM_\star/R_\star} \approx 100 - 200$ km s $^{-1}$, from the stellar surfaces. A key to understand the slow RGB winds is that static regions are formed above the photospheres. The onset of the winds is not from the stellar surfaces but from around several R_\star . This is the main reason why the wind speeds are much smaller than $v_{\text{esc},0}$ (§3.3).

The wind densities are larger in the more evolved stars because the pressure scale heights ($\propto g^{-1}$) are longer and the decreases of the densities becomes slower. Then, the mass flux, ρv_r , increase with the stellar evolution in spite of the decrease of v_r . Accordingly, the mass loss rate, $\dot{M} (\propto \rho v_r R_\star^2)$, increases, cooperating with the expansion of R_\star (§3.4).

The evolution of the stellar wind properties is more clearly illustrated in Figure 4 which shows the typical wind parameters, temperature, T (K) in the atmosphere (top), wind speed, V_{20R_\star} (km s $^{-1}$), at $20 R_\star$ (middle), and $\dot{M} = 4\pi(\rho v^2)_{20R_\star} (M_\odot \text{ yr}^{-1})$ evaluated at $20 R_\star$ (bottom), as functions of $v_{\text{esc},0}$. Note that the

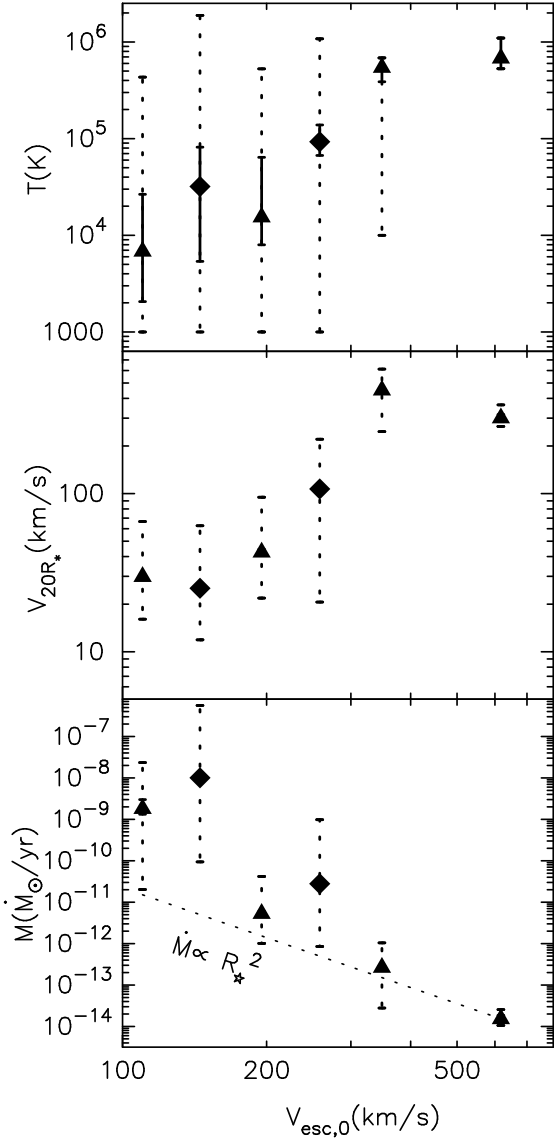


FIG. 4.— Typical wind parameters of the six Models as functions of surface escape velocity, $v_{\text{esc},0}$ (km s^{-1}). The triangles and diamonds represents the results of the $1 M_{\odot}$ (Models I - IV) and $3 M_{\odot}$ (Models V & VI) stars respectively. From the top to the bottom temperature, T (K), outflow velocity, v_{20R_*} at $r = 20 R_*$, and mass loss rate, \dot{M} , evaluated at $r = 20 R_*$ are plotted. T (K) is averaged over the range of $1.5 R_* \leq r \leq 15 R_*$. The solid error bars in the top panel correspond to the maximum and minimum values of the time-averaged structures in this range. The dashed error bars in all the panels correspond to the maximum and minimum values of the snap-shot results (§4).

super-radial expansions of the flux tubes already finish at $r = 20 R_*$. The triangles and diamonds denote the time-averaged results of the $1 M_{\odot}$ (Models I - IV) and $3 M_{\odot}$ (Models V & VI) stars, respectively. In the top panel, we are averaging $T(r)$ in $1.5 - 15 R_*$. The solid error bars correspond to the temperature ranges of the time-averaged structures in this region. The dashed error bars in all the panels correspond to the maximum and minimum values of the snap-shot results (§4).

The top and middle panels shows that both T and v_{20R_*} drop when the star evolves (from the right to the left in Figure 4) across $v_{\text{esc},0} \approx 300 \text{ km s}^{-1}$. The wind character changes from the steady hot and fast wind

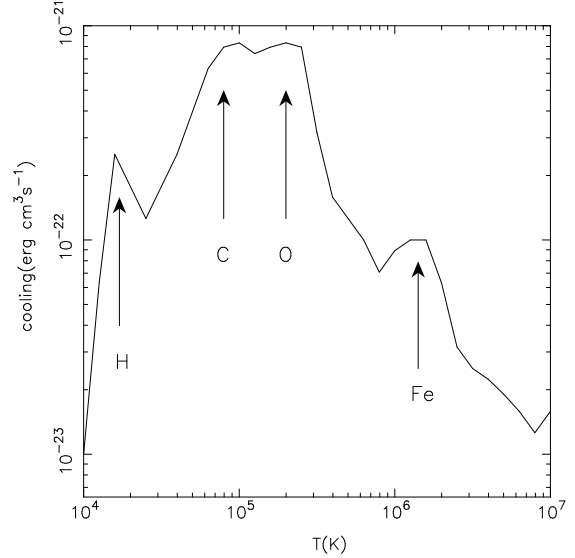


FIG. 5.— Radiative cooling function ($\text{erg cm}^3 \text{s}^{-1}$) for optically thin plasma (Landini & Monsignori-Fossi 1990) as a function of T (K). The main coolants (ions) are indicated by the arrows.

to the fluctuating cool and dense wind. The bottom panel shows that \dot{M} increases rapidly from MS to RGB. In the cases of the $1 M_{\odot}$ stars the average \dot{M} increases by $\simeq (1 - 2) \times 10^5$ times as the star evolves from $\log g = 4.4$ (Model I) to 1.4 (Model IV). Note that \dot{M} of Model IV is comparable to observed values ($\sim 10^{-9} M_{\odot} \text{ yr}^{-1}$) (Judge & Stencel 1991). \dot{M} 's of the $3 M_{\odot}$ stars are systematically larger because both surface areas ($\propto R_*^2$) and mass flux (ρv_r) are larger when measured at the same $v_{\text{esc},0}$. In contrast to the temperature and wind speed, a gap is not seen in \dot{M} around $v_{\text{esc},0} = 200 - 300 \text{ km s}^{-1}$. The increase of \dot{M} is rather conspicuous in $v_{\text{esc},0} \lesssim 200 \text{ km s}^{-1}$, which will be discussed later (§3.4).

3.2. Disappearance of Steady Coronae

Here we explain the disappearance of the steady corona in more detail. As discussed above, the main reason is that the hot corona cannot be confined by the gravity since the sound velocity exceeds the escape velocity. Therefore, the material flows out before heated up to the coronal temperature. However, the temperature gap at $v_{\text{esc},0} \simeq 300 \text{ km s}^{-1}$ (the top panel of Figure 4) cannot be explained only by this reason.

Thermal instability plays an important role in the drop of the temperature. Figure 5 shows radiative cooling function ($\text{erg cm}^3 \text{s}^{-1}$) in $10^4 \text{ K} < T < 10^7 \text{ K}$ of optically thin plasma (Landini & Monsignori-Fossi 1990) used in our simulations. The figure illustrates a peak around 10^5 K which is owing to the cooling via carbon and oxygen ions. As a result, in $T > 10^5 \text{ K}$, the cooling function decreases on increasing T , which indicates that gas is less cooled as it is heated up. This is thermal instability and gas in this temperature range cannot stably exist. In the solar and stellar coronal situation, however, thermal conduction plays a role in stabilization; drastic heating to $T \sim 10^7 \text{ K}$ is suppressed by the downward conduction from the upper corona to the lower chromosphere (Hammer 1982). Then, gas with $T \gtrsim 10^6 \text{ K}$ becomes

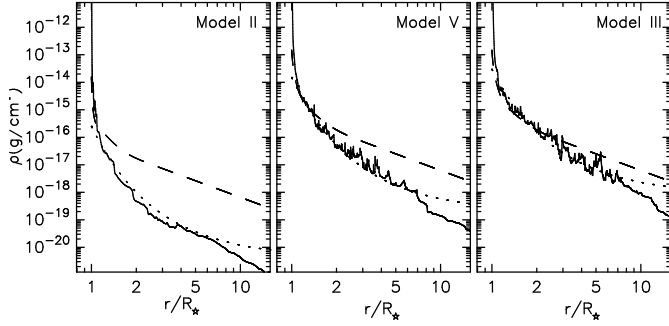


FIG. 6.— Density structures of Model II (left), V (middle), and III (right). The results are the same as in Figure 3 but compared with the densities derived from constant wind speeds (dashed lines) and from hydrostatic structures (dotted lines) (see text).

thermally stable, while gas with $10^5 \text{ K} < T \lesssim 10^6 \text{ K}$ remains unstable.

Let us think about comparison of c_s and v_{esc} at a few R_\star of the $1 M_\odot$ stars. In Models I and II, v_{esc} exceeds c_s ($\simeq 150 \text{ km s}^{-1}$) of 10^6 K plasma. Under such a condition the coronal temperatures are determined by energy balance among heating, radiative cooling, and downward thermal conduction in the transition region which divides the chromosphere and the corona (Hammer 1982). However, in Model III ($\log g = 2.4$), $v_{\text{esc}}(3R_\star) \sim 110 \text{ km s}^{-1}$ and in Model IV ($\log g = 1.4$) $v_{\text{esc}}(3R_\star) \sim 60 \text{ km s}^{-1}$, which correspond to sound speeds of plasmas with $T \simeq 6 \times 10^5 \text{ K}$ and $\simeq 2 \times 10^5 \text{ K}$, respectively. Therefore, the gas streams out before heated up to the stable temperature ($\gtrsim 10^6 \text{ K}$) because of the insufficient confinement by the gravity. Those temperatures are thermally unstable, and then, the actual temperatures become lower than the gravity limited values. This is the reason why the average temperatures of Models III and IV are not 10^5 – 10^6 K but $< 10^5 \text{ K}$. In conclusion, besides the gravity effect the thermal instability gives the sharp decline of the temperature from $T \gtrsim 10^6 \text{ K}$ to $T \lesssim 10^5 \text{ K}$ with the stellar evolution.

The results (Figures 3 & 4) show that the temperatures in the winds of the $3 M_\odot$ RGB stars are systematically higher than those of the $1 M_\odot$ RGB stars. This is because the energy inputs from the surfaces are larger in more massive stars. When fixing surface gravity, a star with a larger mass has higher effective temperature, which gives a larger photospheric amplitude (Equation 9). Then, more energy is injected from the surface so that the larger heating is achieved.

3.3. Wind Speed

The outflow velocity also drastically decreases with the stellar evolution as shown in Figure 4. As briefly stated in §3.1, this is mainly because the wind is accelerated from the effective surface located several R_\star below which the atmosphere stays almost static. We will see this in more detail here. In order to investigate the drastic change, we compare Models near the transition at $v_{\text{esc},0} = 200$ – 300 km s^{-1} (the top panel of Figure 4).

Figure 6 shows the simulated density structures (solid) of Models II (left), V (middle), and III (right), in comparison with the densities derived from assumed constant velocities (dashed) and those of hydrostatic structures

(dotted). The dashed lines plot

$$\rho \propto (r^2 f)^{-1}, \quad (12)$$

which is derived from substituting constant v_r into the continuity equation of mass, $\rho v_r r^2 f = \text{const.}$, under the steady-state condition. The starting point is set in the low chromosphere in each Model.

The dotted lines represent hydrostatic density structures,

$$\begin{aligned} \rho &= \rho_1 \exp \left(\frac{GM_\star}{a_{\text{eff}}^2} \left[\frac{1}{r} - \frac{1}{r_1} \right] \right) \\ &= \rho_1 \exp \left(-\frac{g_1}{a_{\text{eff}}^2} \frac{r_1}{r} z \right), \end{aligned} \quad (13)$$

where r_1 is a certain reference position (not necessarily $r_1 = R_\star$), $z \equiv r - r_1$, $g_1 = GM_\star/r_1^2$, and ρ_1 is the density at $r = r_1$. We here assume “isothermal” atmosphere with effective sound speed, $a_{\text{eff}} \approx a^2 + B_\perp^2/8\pi\rho$, where a is isothermal sound speed; we have to take into account magnetic pressure associated with Alfvén wave in addition to gas pressure. For Models II, V, and III, we adopt $a_{\text{eff}} = 74, 55$, and 43 km s^{-1} , respectively, which are estimated from the simulation results.

Figure 6 shows that the densities in the subsonic (inner) regions can be approximated by the hydrostatic structures, which is consistent with the result of general stellar wind theory (e.g. section 3 of Lamers & Cassinelli 1999). In Model II (the left panel), the dashed line is far above the solid as well as dotted lines, because the scale height is shorter and the decrease of the density is faster due to the stronger gravity. This indicates the acceleration of the wind should start near the surface.

On the other hand, in Models III (the right panel) the decrease of the density is slower thanks to the weaker gravity. As a result, the solid line follows the dashed line in the inner region, which shows that the wind is not accelerated, but stays almost a constant speed. The solid line is gradually diverging from the dashed line around $R_{\text{eff}} \approx \text{several } R_\star$, which we call an “effective” surface, and at which the wind starts to be practically accelerated. In $r \lesssim R_{\text{eff}}$, the average wind speed is kept much slower than 10 km s^{-1} ($\ll c_s$), and the atmosphere is almost static, as seen in Figure 3; the acceleration is not effective there because of too much material. The longitudinal motions seen in this region in the top panel of Figure 3 are not by outflow but due to compressive waves (§3.6). The wind structures of the other RGB stars (Models IV and VI) are essentially similar to that of Model III.

The gravity is smaller at $r = R_{\text{eff}}$ than at the surfaces, hence the slow winds can escape outwardly. Therefore, we can expect that the terminal velocity is not an order of the surface escape speed but an order of the escape speed, $v_{\text{esc}}(R_{\text{eff}}) = \sqrt{GM_\star/R_{\text{eff}}}$, at $r = R_{\text{eff}}$. This can explain why observed wind speeds are much smaller than the surface escape velocities in RGB stars (e.g. Dupree 1986). In Model III we can set $R_{\text{eff}} \simeq 8R_\star$, hence, $v_{\text{esc}}(R_{\text{eff}}) \simeq 70 \text{ km s}^{-1}$. This value is an order of the terminal velocity which is supposed to be slightly faster than the obtained $v_{20R_\star} = 40$ – 50 km s^{-1} when the effect of the acceleration in $r > 20R_\star$ is taken into account.

The situation of Model V (the middle panel) is between Models II and III. The simulated density follows

the trend of non-acceleration at the beginning. However, the solid line departs from the dashed line earlier than in Model III. In this case the wind is gradually accelerated from a few R_\star . The difference between Models III and V is owing to an effect of the different stellar radii. Although these two Models have the same g , R_\star is larger in Model V by $\sqrt{3}$. Then, the decrease of the density is faster in Model V when we measure by r/R_\star ; the density of Model V is smaller than the density at the same r/R_\star of Model III (Equation 13). The acceleration occurs from $R_{\text{eff}} \sim 3 R_\star$ in Model V, not from $R_{\text{eff}} \approx (5 - 10)R_\star$ as in Model III. The wind speed in the outer region is regulated by $v_{\text{esc}} (\sim 150 \text{ km s}^{-1})$ at this $R_{\text{eff}} (\sim 3 R_\star)$, which is an order of the obtained $v_{20 R_\star}$.

In summary, we have the natural conclusion that the wind speed is determined by the escape speed at $r = R_{\text{eff}}$ where the wind practically starts to flow out. R_{eff} does not coincide with the stellar surface but moves outward as a star expands. Therefore, the wind speed of the RGB star is slower than the surface escape speed.

3.4. Mass Loss Rate

The bottom panel of Figure 4 shows the mass loss rates rapidly increase as the stars expand. This is owing to the increases of both stellar surfaces ($\propto R_\star^2$) and mass fluxes (ρv_r). We draw the trend derived from the constant ρv_r by the dotted line started from the result of Model I; if the trend of the $1 M_\odot$ stars (the triangles) followed this line, it would indicate that the increase of \dot{M} is simply due to the gain of the surface area. \dot{M} 's of Models II and III are only slightly above the dotted line, and that the increase of \dot{M} from Model I to Model III is mainly by the geometrical reason.

On the other hand, \dot{M} of Model IV largely exceeds the dotted line. Hence, the increase of the density dominates the R_\star^2 effect from Models III to IV. In evolved stars, wind densities become higher because more materials can be lifted up under the lower gravity environments so that the mass fluxes themselves increase. The increase of the average \dot{M} is $(1 - 2) \times 10^5$ times from Models I to IV. The R_\star^2 effect predicts a 10^3 times increase. Then, the rest of $(1 - 2) \times 10^2$ times increase is owing to the increase of the mass flux. It should be noted that the increase of the density is actually larger by this extent since the wind speed decreases.

A sharp change is not seen in \dot{M} at $v_{\text{esc},0} \sim 300 \text{ km s}^{-1}$ as in the wind speed and temperature (Figure 4). In fact, the density itself increases drastically by ~ 2 orders of magnitude from Models II to III. However, the wind speed drops (§3.3), which compensates the increase of ρ . Then, the increase of \dot{M} seems rather continuous.

\dot{M} of the $3 M_\odot$ stars are larger than \dot{M} of the $1 M_\odot$ stars with the same $\log g$ by ~ 1 order of magnitude. R_\star of a $3 M_\odot$ star is $\sqrt{3}$ times larger than R_\star of a $1 M_\odot$ star (with the same $\log g$), hence, the R_\star^2 effect explains 3 times increase of \dot{M} . Therefore, ρv_r should be also larger by ~ 3 times. The reason of larger ρv_r in the more massive RGB stars is that the input surface amplitudes are larger because the effective temperatures are higher (Equation 9). The energy fluxes of the excited waves are larger, which drives the stronger winds.

It is worth comparing our results with the empirical \dot{M}

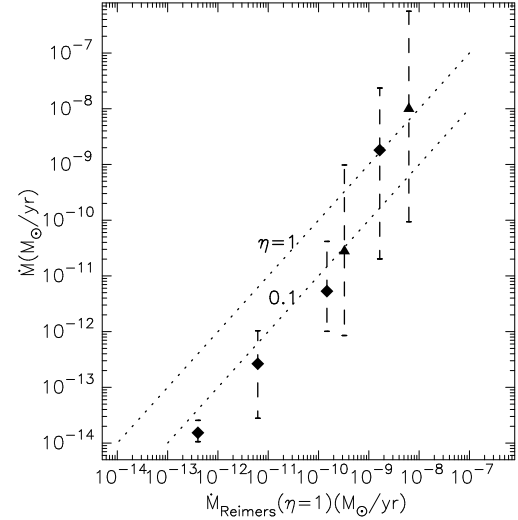


FIG. 7.— Comparison of the mass loss rates (vertical axis) with the Reimers empirical relation (horizontal axis).

relation by Reimers (1975):

$$\dot{M}_{\text{Reimers}} = 4 \times 10^{-13} \eta \frac{(L_\star/L_\odot)(R_\star/R_\odot)}{(M_\star/M_\odot)} (M_\odot/\text{yr}), \quad (14)$$

where η is a proportional coefficient of an order of unity. This is based on a dimensional analysis of stellar wind energetics. Figure 7 compares the obtained \dot{M} with the \dot{M}_{Reimers} with $\eta = 1$. The comparison indicates that the Reimers relation roughly gives reasonable estimates. However, smaller $\eta \lesssim 0.1$ seems to be systematically favored in the higher gravity stars. We explain this tendency from the wind energetics, similarly to the Reimers' arguments.

In our wave-driven wind simulations, the radiation part (L_\star) should be replaced by wave energy in Equation (14). In an open flux tube, a fraction, ϵ , of the initial energy flux of input Alfvén wave is transferred to the stellar wind. This can be written as

$$\epsilon R_\star^2 F_w = r^2 f \rho v_r \frac{v_r^2}{2}, \quad (15)$$

where $F_w = \rho \langle \delta v_0^2 \rangle v_A$ is wave energy flux. The left-hand side is evaluated at the surface and the right-hand side is at a sufficiently distant location at which $f = f_{\text{tot}}$ and $v \approx v_\infty$. Multiplied by 4π , transformation of Equation (15) gives

$$\epsilon L_w = \dot{M} \frac{v_\infty^2}{2}, \quad (16)$$

where $L_w = 4\pi R_\star^2 F_w / f_{\text{tot}}$ is wave luminosity and $\dot{M} = 4\pi \rho v_\infty r^2$. Here F_w / f_{tot} is used instead of F_w because the fraction of the area occupied by open field regions at the surface is $1/f_{\text{tot}}$. Then, \dot{M} has the following relation:

$$\begin{aligned} \dot{M} &= 2\epsilon \frac{L_w}{v_\infty^2} = \left(2\epsilon \frac{v_{\text{esc},0}^2}{v_\infty^2} \frac{L_w}{L_\star} \right) \frac{L_\star}{v_{\text{esc},0}^2} \\ &\propto \left(\epsilon \frac{v_{\text{esc},0}^2}{v_\infty^2} \frac{L_w}{L_\star} \right) \frac{L_\star R_\star}{M_\star}. \end{aligned} \quad (17)$$

Comparison between Equations (14) and (17) indicates that η is controlled by $\left(\epsilon \frac{v_{\text{esc},0}^2}{v_{\infty}^2} \frac{L_w}{L_*}\right)$ in the Alfvén wave-driven wind.

ϵ is $\sim 10^{-2}$ (see Figure 11) whereas we leave detailed discussion until §3.7. $\frac{v_{\text{esc},0}^2}{v_{\infty}^2}$ increases with the stellar evolution since the decrease of v_{∞} is faster than the decrease of $v_{\text{esc},0}$ (§3.3). The rest part becomes

$$\begin{aligned} \frac{L_w}{L_*} &= \frac{F_w/f_{\text{tot}}}{\sigma T_{\text{eff}}^4} = \frac{\rho \langle \delta v_0^2 \rangle (B_0/f_{\text{tot}}) / \sqrt{4\pi\rho}}{\sigma T_{\text{eff}}^4} \\ &\propto \frac{\sqrt{\rho} \langle \delta v_0^2 \rangle}{T_{\text{eff}}^4} \propto g^{-1} T_{\text{eff}}^{7.5}, \end{aligned} \quad (18)$$

where the last proportionality is from Equations (8) & (9), and note that our simulations adopt the same $B_0/f_{\text{tot}} (= 1 \text{ G})$ in all the Models. Along with the stellar evolution, the effect of g dominates that of T_{eff} in Equation (18) because the change of T_{eff} is quite small. Therefore, both $v_{\text{esc},0}^2(R_*)/v_{\infty}^2$ and L_w/L_* terms explain why η is smaller ($\approx 0.01 - 0.1$) in the MS and SB stars and increases to $\approx \text{unity}$ in the RGB stars.

3.5. Chromosphere

As we have shown in Figure 3, the temperatures in the atmospheres are higher than the surface temperatures (T_{eff}). In the MS and SB cases (Models I & II), the steady hot coronae with $T \approx 10^6 \text{ K}$ are formed. In the RGB stars (Models III - VI), the warm regions with $T = 10^4 - 2 \times 10^5 \text{ K}$ are seen. These hot/warm regions and the photospheres are connected by cool chromospheres with $T \lesssim 10^4 \text{ K}$. The chromosphere is important because it determines the basal conditions of the stellar winds. Properties of the chromospheres also evolve with the stellar evolution, which we study in this subsection.

It should be noted that the warm regions in the RGB stars are the only results of the time-average; they are the mixtures of hot ($10^5 - 10^6 \text{ K}$) bubbles and cool ($\lesssim 10^4 \text{ K}$) winds, although we leave detailed discussions until §4. The locations at which the temperatures start to increase in the RGB stars are different from the well-defined coronal bases of the MS and SB stars, but the positions where hot bubbles begin to be created intermittently. Hence, we do not call the warm regions “warm coronae”. Nevertheless, the average properties have systematic trends with the stellar parameters, and it is worth studying changes of such average behaviors with the stellar evolution.

In Figure 8 we show the time-averaged density (top) and temperature (middle) structures which are the same as in Figure 3 but plotted on $(r - R_*)/R_*$ to enlarge the inner regions. Note that the physical distance (e.g. km) of the horizontal axis becomes larger for the star with larger R_* . In the bottom panel plasma β value defined as

$$\beta \equiv \frac{8\pi p}{B^2} \quad (19)$$

is plotted.

The density distributions in the chromospheres are well approximated by hydrostatic structures of given effective sound speeds, a_{eff} (Equation 13). Since a_{eff} ’s in the chromospheres are not so different in the simulated

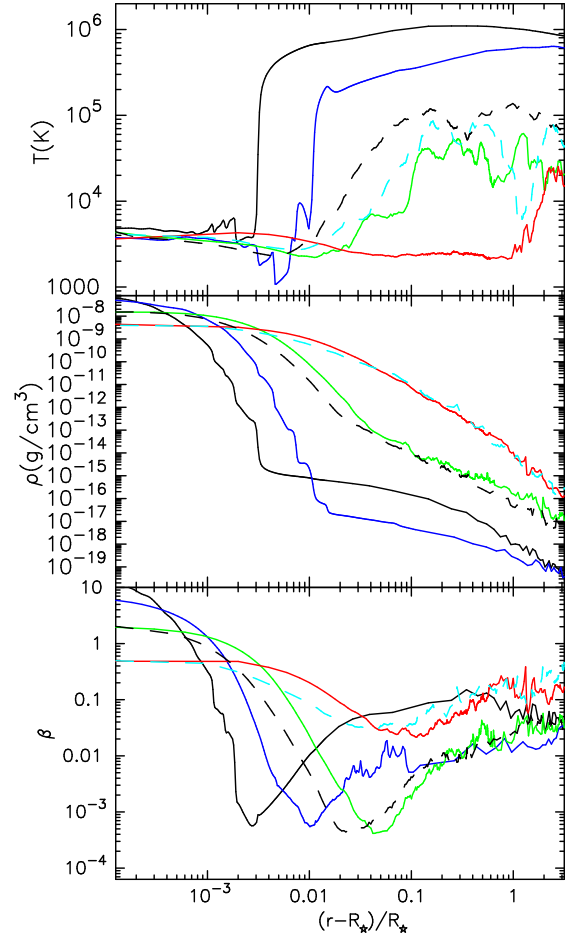


FIG. 8.— Structures of the inner regions of the six Models. From the top to the bottom, T (K), ρ (g cm^{-3}), and plasma β values are shown on $(r - R_*)/R_*$. The results in the top and middle panels are the same as in Figure 3. The solid lines are the results of the $1 M_{\odot}$ stars; the black, blue, green, and red lines are the results of Models I, II, III, and IV, respectively. The dashed lines are the results of the $3 M_{\odot}$ stars; the black and light-blue lines are the results of Models V and VI.

stars, the densities decrease more rapidly in the stars with larger $\log g$. According to the decreases of the densities, β values also decrease, because the decreases of the magnetic pressures are slower than those of the densities. The β values decrease to $\sim 10^{-3}$ in the stars with $\log g = 2.4 - 4.4$, which means that the magnetic pressures dominates the gas pressures by ~ 1000 times. Then, dissipation of a small fraction of magnetic energy gives an enormous effect on the gas; it is heated up quite easily. Indeed, the energy transfer from the magnetic fields to the plasmas is carried by the dissipation of the Alfvén waves in our simulations and the gas is heated up before β becomes further smaller. As the temperatures rise, the decreases of the densities become slower (Equation 13) and β ’s increase due to the decreases of B ’s. The densities at which the temperatures start to increase are controlled in order that the plasma β values do not become too small.

In the stars with the lowest gravity ($\log g = 1.4$), the β values do not become as small as the other stars since the decreases of the densities in the chromospheres are too slow to achieve such small β . Therefore, strong heating

do not occur in these stars and the average temperatures are lower than the stars with the larger $\log g$.

The chromospheres are deeper in the more evolved stars. For instance, in Model IV the chromosphere extends to $r - R_\star \simeq 1 R_\star$, while in Model I it is only up to $r - R_\star = 0.003 R_\star$. They are $\sim 10^4$ times different in physical distance. This is because of the large difference of the scale heights ($\sim a_{\text{eff}}^2 r / g R_\star$). A longer distance is needed for density to decrease by the same extent in a more evolved star.

The physical depths of the chromospheres of the $3 M_\odot$ stars are slightly shallower than those of the $1 M_\odot$ counterparts with the same $\log g$ (though it is not easily seen). This is because the atmospheres of the $3 M_\odot$ stars experience more heating owing to the larger photospheric amplitudes. Then, hot bubbles are heated up in more deeper locations where the densities are higher.

The chromosphere is also important in terms of supply of mass to the corona. Material should be supplied to the upper hotter region to compensate the mass loss by the stellar wind. This means that chromospheric materials should move outwardly to satisfy the mass continuity equation, although its speed is much smaller than the sound speed. In MS and SG stars which have the hot coronae, this outward slow motion in the chromosphere is mainly driven by chromospheric evaporation (Hammer 1982) due to downward thermal conduction from the upper hot coronae. These heated up materials are supplied upwardly into the coronae.

On the other hand, the situation of the RGB stars is different. While a small fraction (in mass) of the chromospheric material is evaporated into hot bubbles which move outwardly, most of it is lifted up by the magnetic pressure of Alfvén waves (without heated up) and directly accelerated as cool chromospheric wind.

3.6. Dissipation of Waves

We have shown that the stellar winds are naturally driven by the turbulent convections of the stellar surfaces in both MS and RGB stars. The key process here is the dissipation of the Alfvén waves which are directly generated by the surface turbulences. In Suzuki & Inutsuka (2005, 2006), we claimed that nonlinear generation of MHD slow (\approx sound) waves is the main dissipation process in our 1D simulation of the solar wind; the energy flux of Alfvén waves is transferred to slow waves which dissipate by shocks after steepening of the wave fronts. We show that the same mechanism operates in RGB stars. We firstly inspect the dissipation processes by using the results of Model III, and after that, we compare the dissipation conditions in the four cases of the $1 M_\odot$ stars (Models I-IV).

Figure 9 plots the following adiabatic constants derived from wave action (Jacques 1977),

$$S_c = \rho \langle \delta v_w^2 \rangle \frac{(v_r + v_{\text{ph}})(v_r + v_{\text{ph}})}{v_{\text{ph}}} \frac{r^2 f(r)}{r_c^2 f(r_c)}, \quad (20)$$

for outgoing Alfvén, incoming Alfvén, and outgoing slow MHD (sound) waves of Model III as functions of distance, where δv_w and v_{ph} are amplitude and phase speed of each wave mode. The outgoing and incoming Alfvén waves are decomposed by correlation between v_\perp and B_\perp . Extraction of the slow wave is also from fluctuating components of v_r and ρ . The subscript, c , denotes

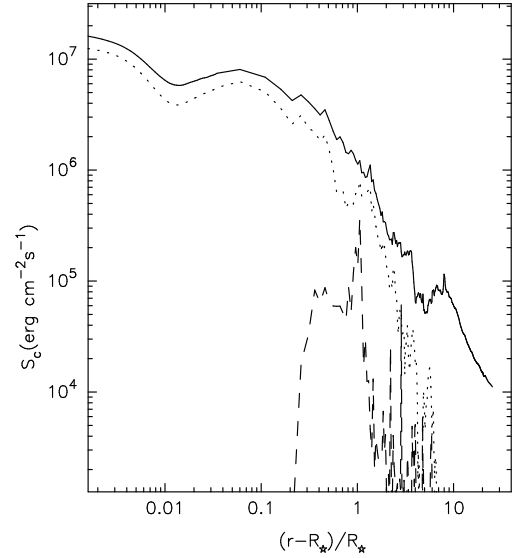


FIG. 9.— Adiabatic constants, S_c 's ($\text{erg cm}^{-2}\text{s}^{-1}$), of outgoing Alfvén (solid), incoming Alfvén (dotted), and outgoing slow MHD waves in Model III.

that S is normalized at r_c where the flux tubes expand by $f_c = 40$, to compensate the effect of the adiabatic loss. S_c can be used as a measure of the dissipation. Although S_c and energy flux are identical in static media, they are not in moving media. S_c is conserved in expanding atmosphere if the wave does not dissipate, while it is not the case for the energy flux. For the incoming Alfvén wave, we plot the opposite sign of S_c so that it becomes positive in the sub-Alfvénic region.

Figure 9 shows that the outgoing Alfvén waves dissipate quite effectively; $S_c (= |S_c|)$ becomes only $\sim 10^{-3}$ of the initial value at the outer boundary. First, a sizable amount is reflected back quite near the surface, which is clearly illustrated as the incoming Alfvén wave following the outgoing component with slightly smaller level. This is because the wave shape is considerably deformed owing to the steep density gradient. In this region, the temperature is small, $T \simeq 3000$ K, which gives a short pressure scale height, H_P . Then, the wavelength of the Alfvén waves becomes comparable or longer than H_P , which results in effective reflection of the waves (Moore et al. 1991). In this Model III, more than 60% of the initial energy flux of the Alfvén waves are reflected back before reaching the upper warm region with the average temperature, $\sim 10^5$ K (§3.7).

Second, slow MHD waves are generated in the corona (see Sakurai 2002 for solar observation) as shown in Figure 9. The generation of the slow waves is by variation of magnetic pressure, $B_\perp^2 / 8\pi$, accompanying with the Alfvén waves (Kudoh & Shibata 1999). This excites density perturbations, which are slow MHD waves in magnetically dominated plasma. Slow waves are generally longitudinal, and then, they eventually suffer nonlinear steepening to lead to the shock dissipation (Suzuki 2002). Density fluctuations of slow waves also work as mirrors to Alfvén waves. The variation of the density directly leads to the variation of the Alfvén speeds ($\propto B / \sqrt{\rho}$), which enhances the reflection of the Alfvén waves by the deformation of the shape.

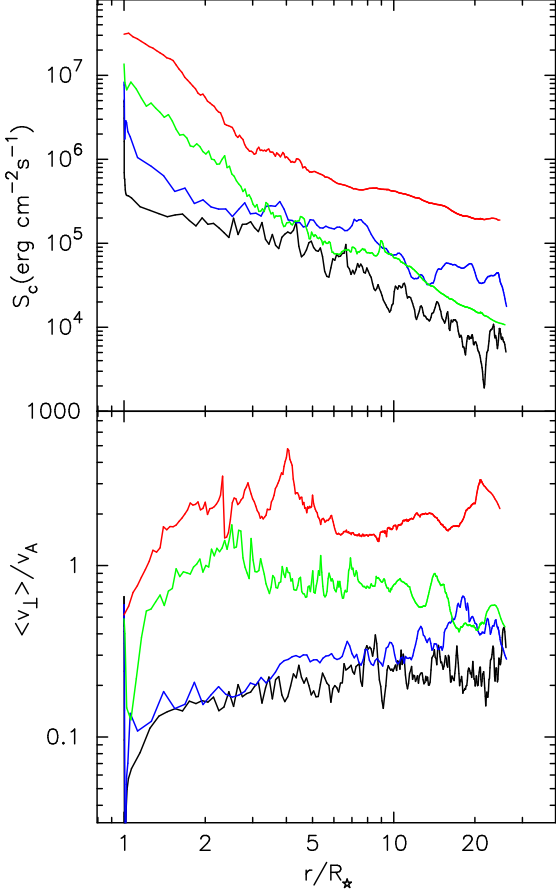


FIG. 10.— Properties of Alfvén waves in the $1 M_{\odot}$ stars (Models I - IV). The top panel exhibits the adiabatic constant, S_c , and the bottom panel shows the nonlinearity, $\langle v_{\perp} \rangle / v_A$. The black, blue, green, and red lines are the results of Models I, II, III, and IV, respectively.

The process discussed here is the parametric decay instability of Alfvén waves due to three-wave (outgoing Alfvén, incoming Alfvén, and outgoing slow waves) interactions (Goldstein 1978; Terasawa et al. 1986). The decay instability is not generally efficient in the homogeneous background since it is a nonlinear mechanism. Therefore, it has not been considered as a major process of the acceleration of the solar and stellar winds. However, the density gradient of the background plasma totally changes the situation. In addition to the reflection mentioned above, the amplification of the wave amplitude enhances the dissipation of Alfvén waves. The velocity amplitudes of Alfvén waves are amplified because of the rapid decrease of the density. Although the Alfvén speed ($\propto B/\sqrt{\rho}$) also increases initially in the low chromosphere, it decreases because of the expansion of the flux tube (the decrease of B). As a result, nonlinearity ($\langle v_{\perp} \rangle / v_A$) increases as Alfvén waves travel upward (see Figure 10), which leads to efficient dissipation.

Figure 10 compares the dissipation of the Alfvén waves in the four Models of the $1 M_{\odot}$ stars. In the upper panel S_c 's are compared, and in the lower panel nonlinearities, $\langle v_{\perp} \rangle / v_A$, are shown, where $\langle v_{\perp} \rangle = \sqrt{\langle v_{\perp}^2 \rangle}$. The figure shows that the wave energies drastically attenuate just above the surfaces in the stars with higher gravity because of the reflection in the chromospheres.

In these stars the densities decrease more rapidly in the chromospheres, leading to the increases of v_A 's. Then, the wavelength of the Alfvén wave with the typical frequency (e.g. several min. in Model I) becomes longer than $H_p \sim a_{\text{eff}}^2/g$ which itself is substantially smaller for larger $\log g$. This enhances the reflection as explained above.

Besides this effect, in the stars with the larger $\log g$, the chromospheres are geometrically thin ($r - R_{\star} \ll R_{\star}$). Otherwise if the chromosphere extends to $r - R_{\star} \gtrsim R_{\star}$ as in the RGB stars, a curvature effect increases H_p by r/R_{\star} (Equation 13), which reduces the wave reflection. This is also a reason why the reflection becomes relatively important in the higher gravity stars. Finally, less than half of the input wave energies can penetrate into the warm/hot regions in Models I - III (§3.7).

Let us turn to the waves in the outer regions. Wave dissipation is more rapid in the stars with lower gravity. This is because the densities in the atmospheres are larger in those stars due to the longer H_p and accordingly Alfvén speeds, $\propto 1/\sqrt{\rho}$, becomes slower. In such a condition Alfvén waves more easily become nonlinear ($\langle v_{\perp} \rangle / v_A \gtrsim 1$ in the bottom panel of Figure 10), which enhances the wave dissipation. It might be expected that the wave energies are more effectively transferred to the winds in the evolved stars. However, the situation is not so simple because in these stars radiative losses become efficient due to the larger densities. We study the wind energetics to discuss these issues in the next subsection.

Before moving on to the next topic we would like to remark on dissipation lengths of the Alfvén waves. In order to avoid complicated dissipation processes of Alfvén waves, phenomenological approach has been often adopted to treat Alfvén waves in solar and stellar wind models (e.g. Hartmann & MacGregor 1980); action of Alfvén waves is assumed to follow

$$S \propto \exp\left(-\frac{r - R_{\star}}{l}\right), \quad (21)$$

where l is a (constant) dissipation length ($= 0.1 - 10 R_{\star}$). We can directly estimate l from our simulations. The upper panel of Figure 10 illustrates that the decreases of S_c are more or less straight in the $\log(r/R_{\star}) - \log S_c$ diagram. This means that the dissipation lengths increase on r . For example, the dissipation length of Model IV is $\lesssim 1 R_{\star}$ in $r < 3 R_{\star}$, but it becomes $\approx 10 R_{\star}$ in $r > 10 R_{\star}$. Therefore, the assumption of a constant dissipation length is not appropriate.

3.7. Wind Energetics

In the previous subsection, we have inspected the dissipation of the Alfvén waves. A certain fraction of the initial wave energy is used for the acceleration of the stellar winds, while the rest of them is lost by radiation and returned back to the stellar surface by outer propagating waves. Although some portions are carried by waves, enthalpy, and thermal conduction away from the outer boundaries, we do not discuss them in detail because their contributions are smaller. We estimate kinetic energy fluxes of the stellar winds at the outer boundaries, integrated radiative loss, and wave energy flux leaking inward from the stellar surfaces, in unit of 1/s :

$$(\rho v_r \frac{v_r^2}{2} f r^2)_{\text{out}}, \quad (22)$$

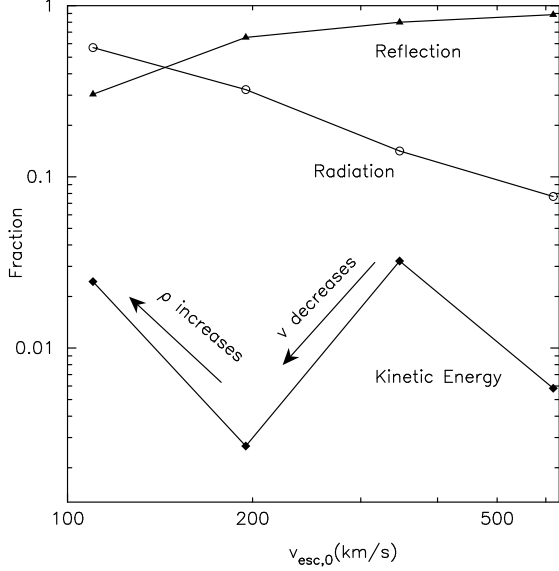


FIG. 11.— The fractions of wind kinetic energy, radiative loss, and wave energy reflected back to the surfaces of the $1 M_{\odot}$ stars as functions of $v_{\text{esc},0}$ (km s^{-1}). Each component is normalized by the input energy flux of the Alfvén waves.

$$\int_{R_*}^{r_{\text{out}}} dr r^2 f q_R, \quad (23)$$

$$(\rho \langle \delta v_{\perp,-}^2 \rangle v_A)_{*} R_*^2, \quad (24)$$

where $\delta v_{\perp,-}$ denotes amplitude of incoming Alfvén waves, and subscripts ‘*’ and ‘out’ indicate that the values are evaluated at the stellar surfaces and the outer boundaries, respectively. Figure 11 presents these energies normalized by the input energy fluxes from the surfaces,

$$(\rho \langle \delta v_0^2 \rangle v_A)_{*} R_*^2, \quad (25)$$

as functions of $v_{\text{esc},0}$.

As one can see, the fractions of the wave energy which are converted to the wind kinetic energy are small. Typically, only $\sim 1\%$ of the surface turbulent energy is transferred to the stellar winds. However, these fractions are enough to keep the observed \dot{M} and $v_{\infty} \approx v_{20R_*}$ of winds from MS and RGB stars.

Most of the energy is lost by the radiation and the wave reflection. In the MS and SB stars, the energy losses are dominated by the wave reflection as discussed in §3.6; the densities decrease more rapidly because of the higher gravity, and then, the wavelengths become longer than the scale heights, which results in the effective reflection via the deformation of the wave shape. The rapid decreases of the densities also make the radiative cooling less effective; it is important only in the chromospheres ($T < 10^4$ K) and low coronae where the densities are sufficiently high (volumetric radiative cooling is $\propto \rho^2$ in optically thin and $\propto \rho$ in optically thick gas). This also leads to the relative dominance of the wave reflection in the total energy loss. On the other hand, the radiative cooling becomes dominant in the evolved star (Model IV) since the decrease of the density is more gradual; the Alfvén waves less suffer the reflection and the radiative loss is efficient even in the outer region because the density is still high.

Let us turn back to the kinetic energy part. The tendency on $v_{\text{esc},0}$ is not monochromatic. As the star evolves from MS phase ($v_{\text{esc},0} = 617 \text{ km s}^{-1}$) to SB ($v_{\text{esc},0} = 347 \text{ km s}^{-1}$), the fraction of the kinetic energy increases mainly because the mass flux, ρv_r , increases. However, the fraction of the kinetic energy drops almost by one order of magnitude from Models II to III ($v_{\text{esc},0} = 195 \text{ km s}^{-1}$). This is because of the drastic decrease of the wind speed (Figure 4). Although the density increases from Models II to III, the effect of the velocity dominates since the kinetic energy flux is proportional to ρv_r^3 . From Models III to IV ($v_{\text{esc},0} = 110 \text{ km s}^{-1}$), the decrease of v_r is small, and the fraction of the kinetic energy again increases simply by the increase of the density.

4. HYBRID RGB WINDS –TIME-DEPENDENCY–

In this section we examine time-dependent aspects of the RGB winds. We firstly study Model VI ($3 M_{\odot}$) which is slightly redward of the DL but more active than the $1 M_{\odot}$ counterpart (Model IV). After that, we discuss the other RGB cases.

4.1. Multi-phase Wind

Figure 12 shows the snap-shot wind structures of Model VI at $t = 6909$ (hr) (solid) in comparison with the time-averaged one (dashed) which is the same as in Figure 3. The mpeg movie of the simulation is also available in the *electronic edition*. Figure 12 illustrates that the simple picture of layered atmosphere, photosphere – chromosphere – transition region – corona – wind from below, does not hold in the RGB star. An characteristic feature is that a number of hot bubbles with low densities are distributed in the cool background material. For example, in the inner region ($r - R_* < R_*$) the two bubbles with the peak temperatures $> 10^6$ K are seen; in $R_* < r - R_* \lesssim 10 R_*$ a couple of warm bubbles with $T \gtrsim 10^5$ K are formed. The hot and warm bubbles and the cool background materials are connected by the transition regions at which the temperature drastically changes because of the thermal instability.

The densities of the hot bubbles are lower than the ambient media to satisfy the pressure balance, whereas strictly speaking magnetic pressure also needs to be taken into account (§4.2). Accordingly, the density structure in the wind shows many fluctuations. The RGB stellar wind is not a steady outward stream but an outflow consisting of many small-scale structures. Our simulation shows that both hot plasma and cool chromospheric wind coexist in the RGB star, which is consistent with observations of hybrid stars (Hartmann, Dupree, & Raymond 1980; Ayres et al. 1998).

4.2. Magnetized Hot Bubble

How are these hot bubbles formed? How are the high temperatures maintained? We study formation and evolution of bubbles by inspecting one typical hot bubble which is indicated by the arrows in Figure 12. This bubble is initially created at $r = 1.04 R_*$ at $t = 6755$ hr. It comoves outwardly with the background flow and eventually cooled down to $\approx 10^4$ K at $t \approx 7070$ hr at $r = 1.6 R_*$ (see the mpeg movie of Figure 12 which is available in the *electronic edition*).

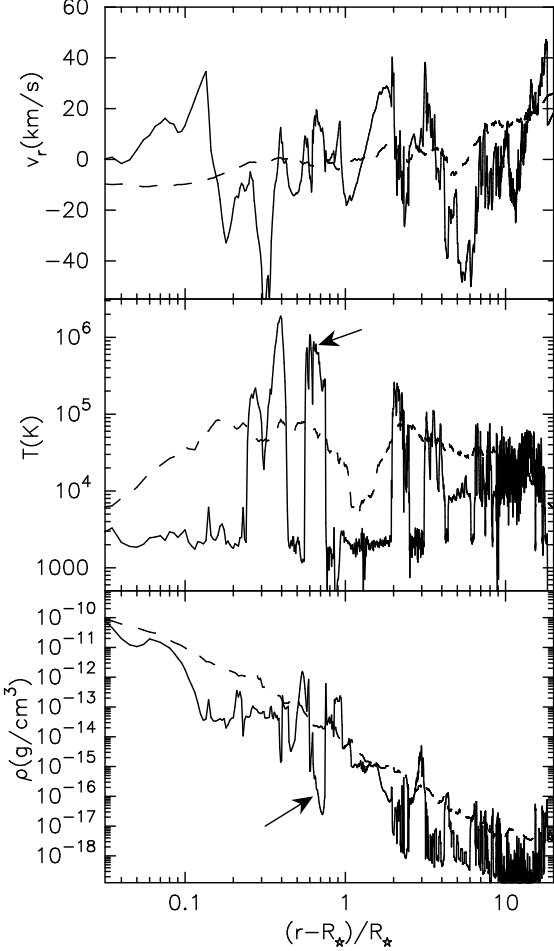


FIG. 12.— Snap-shot result (solid) of stellar wind structure of Model VI at $t = 6909$ (hr), compared with the time-averaged structure (dashed). From the top to the bottom, v_r (km s $^{-1}$), T (K), and ρ (g cm $^{-3}$) are plotted on $(r - R_*)/R_*$. The arrows in the middle and bottom panels show the magnetized hot bubble which we inspect in §4.2 and Figure 13. The mpeg movie which shows this simulation from $t = 0$ to 9800 hr is available in the *electronic edition*. The movie file presents $\langle v_{\perp} \rangle$ (km s $^{-1}$) in addition to v_r (km s $^{-1}$), T (K), and ρ (g cm $^{-3}$).

Figure 13 presents the zoomed-in structures just after the formation of the bubble. In the upper panel magnetic pressure, $p_B = B_{\perp}^2/8\pi$ (dashed; right axis), gas pressure, p (dash-dotted; right axis), and radial velocity, v_r (solid; left axis) are plotted; in the lower panel temperature, T (solid; left axis) and density, ρ , (dashed; right axis) are shown. The location of the shock front is indicated by the dotted line at $r = 1.047 R_*$, and the left side corresponds to the downstream region. p_B increases at the shock front, which indicates that this is fast MHD shock.

The material is concentrated in the narrow region just behind the shock front, which is seen as the density peak there. This is because an effective ratio of specific heats is small $\gamma_{\text{eff}} \lesssim 1.1$ owing to the thermal conduction; the density jump at the shock becomes large in small γ_{eff} circumstances so that the density should be concentrated behind the shock to satisfy the mass conservation (Kim & Ryu 2005). As a result, the gas is effectively cooled down by the radiative loss to $\lesssim 10^4$ K there by the high density; we call this region cool dense shell (Fig-

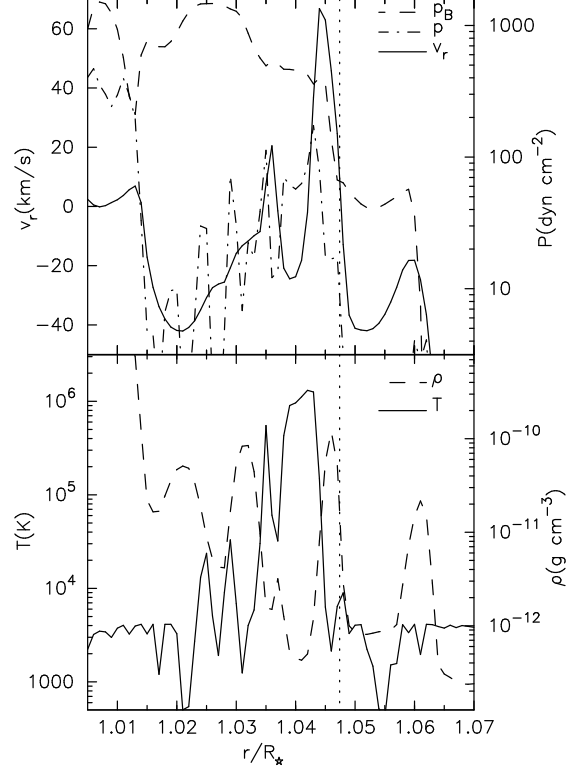


FIG. 13.— Zoomed-in structure of the magnetized hot bubble at $t = 6755$ (hr) which is the initial phase of the bubble indicated by the arrows in Figure 12. The dotted lines show the location of the shock front. *Upper* : The dashed, dot-dashed, and solid lines are magnetic pressure, p_B , gas pressure, p , and radial velocity, v_r . The values of p and p_B are on the right axis (dyn cm $^{-2}$) and the value of v_r is on the left axis (km s $^{-1}$). *Lower* : The solid and dashed lines are temperature (K; left axis) and density (g cm $^{-3}$; right axis).

ure 14).

Behind this cool dense shell the hot region remains which was heated up by the fast MHD shock because the radiative cooling is inefficient due to the low density there (Figure 13). The fast MHD shock plays an important role in maintaining this hot bubble. Because the magnetic field is generated by the shock, the magnetic pressure in the bubble is larger than in the ambient gas. The hot bubble is not supported by the gas pressure but by the magnetic pressure. Then, even though the temperature decreases by some reasons, the bubble can avoid being compressed. The density is kept low to reduce the radiative loss. Therefore, hot bubbles created by fast MHD shocks can generally survive a long time until the magnetic topologies change.

Let us estimate the energy budget of the hot bubble. The cooling efficiency at $T = 10^6$ K is $\Lambda \approx 10^{-22}$ erg cm 3 s $^{-1}$, and then, the cooling rate is

$$q_R = n_p n_e \Lambda \approx 10^{-6} \text{ erg cm}^{-3} \text{s}^{-1} \left(\frac{\rho}{2 \times 10^{-16} \text{ g cm}^{-3}} \right)^2, \quad (26)$$

where we use $\rho = 2 \times 10^{-16}$ g cm $^{-3}$, corresponding to $n_p \approx n_e \approx 10^8$ cm $^{-3}$, as a typical density of the bubble in Figure 12. The cooling time is estimated from this q_R and the energy density, $e = \frac{1}{\gamma-1} p \approx$

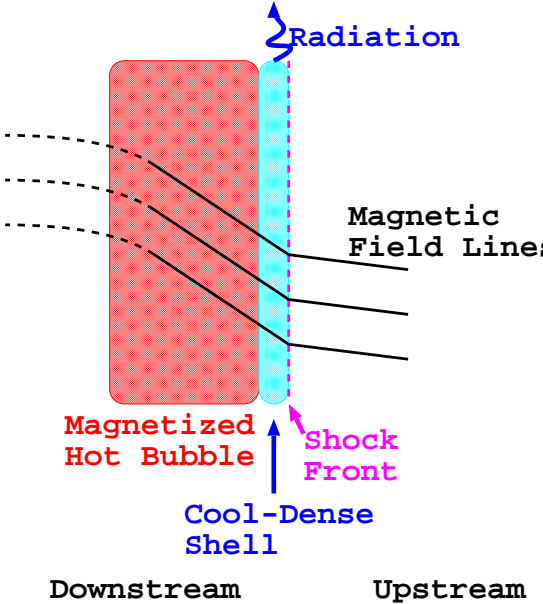


FIG. 14.— Schematic picture of the magnetized hot bubble. Black lines denote magnetic field lines. Magnetic field is amplified at the fast MHD shock (the pink dashed line) and the field strength in the downstream region is larger (note that distance between neighboring lines denotes the strength). The light blue region corresponds to the cool dense shell which cools down by the efficient radiative loss. The red region is the magnetized hot bubble.

$$3 \times 10^{-2} \left(\frac{\rho}{2 \times 10^{-16} \text{ g cm}^{-3}} \right) \left(\frac{T}{10^6 \text{ K}} \right) \text{ erg cm}^{-3}, \text{ as}$$

$$\tau_{\text{cool}} = e/q_R$$

$$\approx 10 \text{ hr} \left(\frac{\rho}{2 \times 10^{-16} \text{ g cm}^{-3}} \right)^{-1} \left(\frac{T}{10^6 \text{ K}} \right)^{-1} \quad (27)$$

This τ_{cool} is much shorter than the lifetime ($= 315 \text{ hr}$) of the hot bubble, which indicates that continuous heating is required to keep $T \gtrsim 10^6 \text{ K}$.

The average outward speed of the bubble ($\sim 10 \text{ km s}^{-1}$) is much slower than the Alfvén speed ($\gtrsim 100 \text{ km s}^{-1}$), hence, many Alfvén(ic) wave trains which pass through the bubble play a role in the heating. The average heating rate can be estimated by

$$q_H \simeq \frac{B_{\perp}^2}{8\pi} \frac{v_A}{l}$$

$$\approx 10^{-6} \text{ erg cm}^{-3} \text{ s}^{-1} \left(\frac{B_{\perp}}{3G} \right)^2 \left(\frac{v_A}{100 \text{ km s}^{-1}} \right) \left(\frac{l}{R_*} \right)^{-1} \quad (28)$$

where l is (average) dissipation length $\sim R_*$ which is derived from the decrease of S_c (e.g. Figure 9 for Models I - IV), and the averaged values at $r \simeq 1.5 R_*$ are adopted for B_{\perp} and v_A . Comparison between Equations (26) and (28) shows that the wave heating can sufficiently balance with the radiative cooling in the hot bubble. The most important point is that thanks to the magnetic pressure the density is kept low enough to reduce the radiative loss. Without the magnetic support the density would increase by compression, and the bubble would quickly cool down with timescale of $\sim \tau_{\text{cool}}$. The fast shock structure plays the major role in sustaining the hot bubble.

An intriguing concept of the magnetized hot bubble is that hot plasma can be heated up even in open field regions. It has been generally considered that closed loop

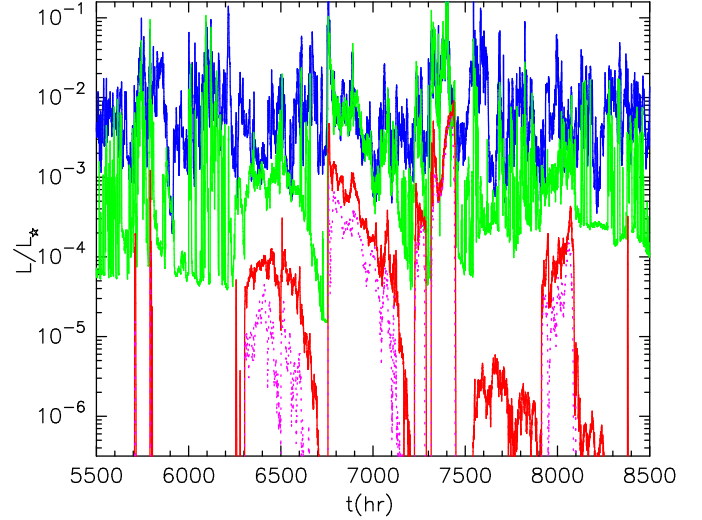


FIG. 15.— Normalized radiative fluxes, L/L_* , of cool ($T \leq 2 \times 10^4 \text{ K}$; blue), warm ($2 \times 10^4 < T < 5 \times 10^5 \text{ K}$; green), and hot ($T \geq 5 \times 10^5 \text{ K}$; red) components of Model VI as functions of time elapsed from the beginning of the simulation. The radiative flux of $T \geq 10^6 \text{ K}$ gas, which is a part of the hot component, is also plotted (dashed line).

structures are necessary to confine hot plasma in the atmosphere of a RGB star since the gravity is not sufficiently strong. However, our simulations show that the hot bubble can exist rather long time (~ 10 days) by magnetic topology, *i.e.* fast MHD shock, in open field regions. It is supposed that such hot bubbles are ubiquitously created and they are possible sources of continuous soft X-ray emissions in hybrid stars as discussed later (§4.3).

4.3. Radiative Flux

The hot bubbles in the RGB atmospheres become sources of soft X-ray and extreme UV (EUV) radiation which is observed in hybrid stars. We present radiative fluxes, normalized by the bolometric luminosity, from the entire star of Models VI as functions of time in Figure 15. Blue, green and red lines are the radiative flux from gas with $T \leq 2 \times 10^4 \text{ K}$ (optical; chromosphere), $2 \times 10^4 \text{ K} < T < 5 \times 10^5 \text{ K}$ (UV; transition region) and $5 \times 10^5 \text{ K} \leq T$ (EUV/soft X-ray; corona). We call them cool, warm, and hot components, respectively. We also plot the radiative flux of the gas with $T \geq 10^6 \text{ K}$ which is a part of the hot component and corresponds to soft X-ray emission.

When deriving the radiative fluxes from the entire star, we assume spherical symmetry:

$$L(T_1 < T < T_2) = 4\pi \int dr r^2 q_R(T_1 < T < T_2), \quad (29)$$

where T_1 and T_2 are the minimum and maximum temperatures of each component. While our simulations only treat the open magnetic field regions, in reality a certain fraction of the surface is covered by closed structures. Equation (29) assumes that the radiative fluxes from both open and closed regions have the same r dependence. Although this treatment is not strictly correct, we can give rough estimates.

According to Figure 15, the hot component shows strong intermittent activities, while the cool component,

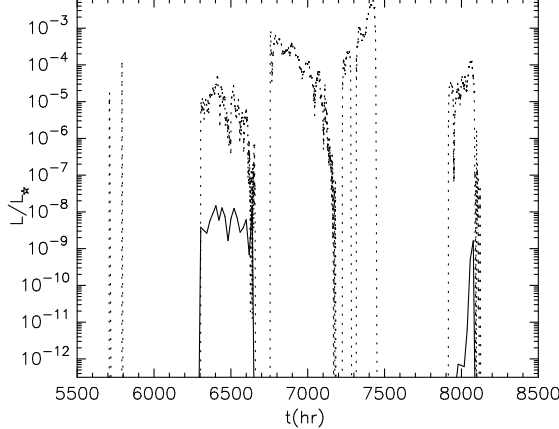


FIG. 16.— The radiative flux of soft X-ray ($T \geq 10^6$ K) which takes into account the absorption by the cool wind materials (solid), in comparison with the original flux without the absorption (dashed).

which dominates the total radiative flux, stays roughly constant within $10^{-3} \lesssim L_{\text{cool}}/L_\star < 10^{-1}$. The behavior of the warm component is between the cool and hot ones; when the hot component is switched-off or stays in low activity phases (e.g. 7500 – 8000 hr) $L_{\text{warm}}/L_\star \approx 10^{-4}$, but once the hot component becomes active, L_{warm}/L_\star increases to $\gtrsim 10^{-2}$ by the contributions from the transition regions of hot bubbles.

Figure 15 also shows that the hot bubbles with $T \geq 10^6$ K exist during the only half of the presented duration. However, we should note that this is based on the approximation of the spherical symmetry. In reality, hot bubbles are created in different open flux tubes at different times. Probably, hot bubbles are ubiquitously distributed in the atmosphere, and they would be the continuous soft X-ray sources.

4.3.1. Absorption of X-ray by Chromospheric Wind?

The integration of the soft X-ray flux ($T \geq 10^6$ K; dotted line) of Figure 15 with time gives the average $\overline{L_X/L_\star} \approx 10^{-4}$. Although this value largely exceeds the observed level $\lesssim 10^{-7}$ of hybrid stars (e.g. Ayres 2005), we need to take into account the absorption of the X-ray by the cool chromospheric materials in the outer region to estimate the observed flux. Most of the hot bubbles are distributed in the inner regions ($r \lesssim 2 R_\star$), and the outer regions are mainly occupied in mass by cool winds with $T \lesssim 10^4$ K. The X-ray emissions from the bubbles will be absorbed by Hydrogen in those cool materials.

In Figure 16 we compare the observed soft X-ray flux from the materials with $T \geq 10^6$ K which takes into account the absorption (solid) with the original flux (dashed). Tenfold obscuration of the soft X-ray emissions sets in at column density, $N_{\text{H}} = 5 \times 10^{20} - 5 \times 10^{21} \text{ cm}^{-3}$. We adopt the most optimistic case of $N_{\text{H}} = 5 \times 10^{21} \text{ cm}^{-3}$:

$$L = \int dr r^2 q_{\text{R}} 10^{-N_{\text{H}}/5 \times 10^{21} \text{ cm}^{-3}}. \quad (30)$$

When deriving N_{H} from the simulation result, we only consider the gas with $T < 8000$ K to pick up neutral Hydrogen and assume the solar abundance. Figure 16 illustrates that the most of the soft X-ray emissions are

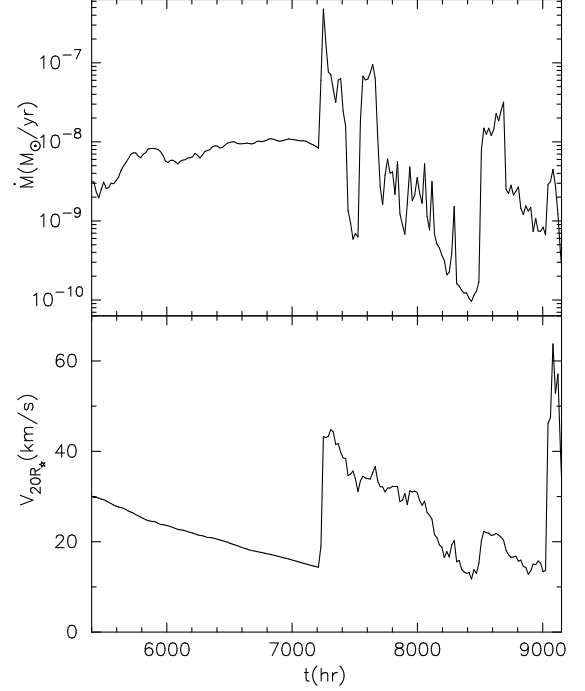


FIG. 17.— The mass loss rate (upper) and radial velocity (lower) of the stellar wind of Model VI as functions of time. Both quantities are evaluated at $r = 20 R_\star$.

absorbed. Around $T \simeq 6500$ and 8000 hr, the soft X-ray could be observed, and the L_X/L_\star is reduced to $\lesssim 10^{-8}$ from $10^{-5} - 10^{-4}$. Interestingly, this value, $L_X/L_\star \lesssim 10^{-8}$, is typical for hybrid stars. However, our calculation, which is based on 1D and do not consider detailed radiative processes, is too simplified for further quantitative arguments.

4.4. Time-Variation of Wind Parameters

Because the RGB stellar wind consists of many small-scale structures, the mass loss rate and the outflow speed in the outer region also show time-dependent behaviors. Figure 17 presents \dot{M} ($M_\odot \text{ yr}^{-1}$) (upper) and wind speed, $v_{20 R_\star}$ (km s^{-1}) (lower) measured at $r = 20 R_\star$. The top panel shows \dot{M} varies more than three orders of magnitude from 1×10^{-10} to $5 \times 10^{-7} M_\odot \text{ yr}^{-1}$. $v_{20 R_\star}$ also varies from 10 km s^{-1} to 60 km s^{-1} .

The jumps are seen in \dot{M} and $v_{20 R_\star}$ at $t = 7200, 8750$, and 9020 hr. These jumps indicate that dense blobs pass at $r = 20 R_\star$ at those times. We examine one of the blobs which passes at $t = 7200$ hr (This is seen in Figure 12 as well). This is a shock wave originally formed in the inner region. The shock amplitude was initially small, but it grows as the shock moves outward by sweeping-up a number of smaller shocks as well as by amplification in the stratified atmosphere with the decreasing density. Finally the compression ratio of the shock increases to more than 10. Note that this value exceeds the adiabatic limit = 4 since our simulations which take into account cooling and thermal conduction are not adiabatic. Before this shock arrives, \dot{M} is almost constant and $v_{20 R_\star}$ shows smoother feature. After the shock reaches, both \dot{M} and $v_{20 R_\star}$ show fluctuating behaviors. This is because the downstream region contains larger perturbation than the

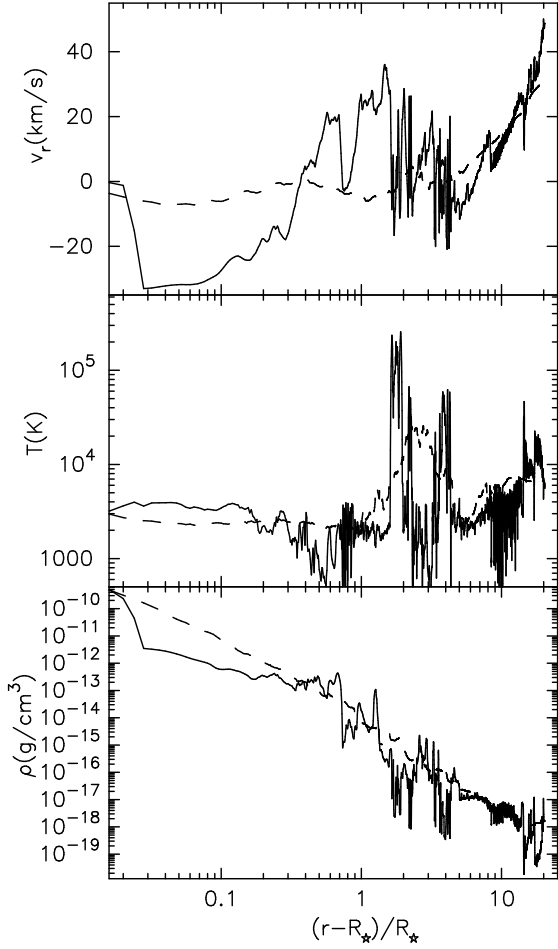


FIG. 18.— Same as Figure 12 but for Model IV at $t = 6050$ hr.

upstream region.

4.5. Dependence on Stellar Masses

We have examined the time-dependent behaviors of the wind from the $3 M_\odot$ RGB star (Model VI). In this subsection we study the $1 M_\odot$ stars on both blueward (Model III) and redward (Model IV) of the DL. Figures 18 and 19 show snap-shot results (solid) of Models IV and III in comparison with the time-averaged results (dashed). Both figures show that the wind structures are not smooth, similarly to Model VI. The atmospheres and winds consist of many hot and warm bubbles and cool chromospheric materials. These figures confirm that RGB winds are generally structured with many blobs and bubbles.

Figures 18 and 19 indicate that the temperatures of the bubbles in Model IV are systematically lower than those of Model III. This trend is clearly seen in the plots of the radiative fluxes in Figure 20 and 21. The emission from the hot gas ($T > 5 \times 10^5$ K) is during the only short term ($t = 5800$ hr) in Model VI, while the hot bubbles with $T > 5 \times 10^5$ K almost always exist in Model III. Then, this indicates that once a star with $1 M_\odot$ crosses the DL, EUV/soft X-ray emissions from hot plasma with $T > 5 \times 10^5$ K happen to disappear. However, the qualitative features of the atmospheres and winds, namely hot/warm bubbles in cool materials, are similar in Mod-

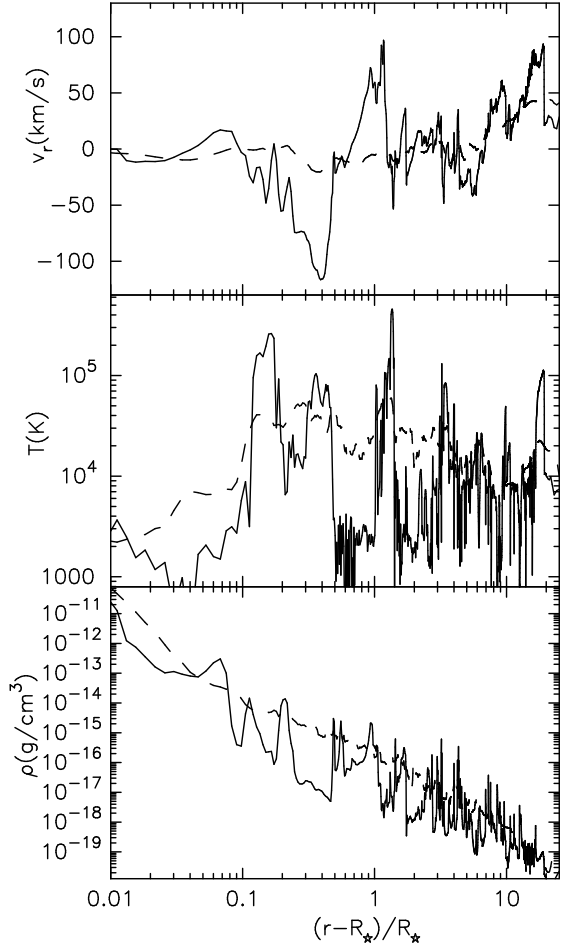


FIG. 19.— Same as Figure 12 but for Model III at $t = 1295$ hr.

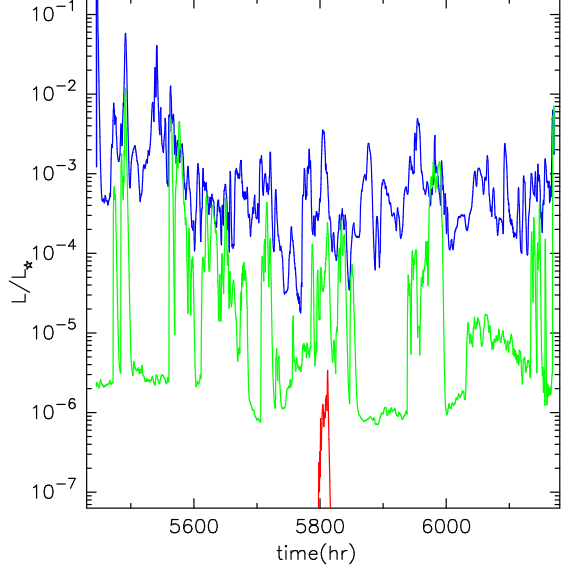


FIG. 20.— Normalized radiative fluxes, L/L_* , of cool ($T \leq 2 \times 10^4$ K; blue), warm ($2 \times 10^4 < T < 5 \times 10^5$ K; green), and hot ($T \geq 5 \times 10^5$ K; red) components of Model IV as functions of time.

els III and IV. The temperatures of the bubbles simply decrease through the evolution from Models III to IV.

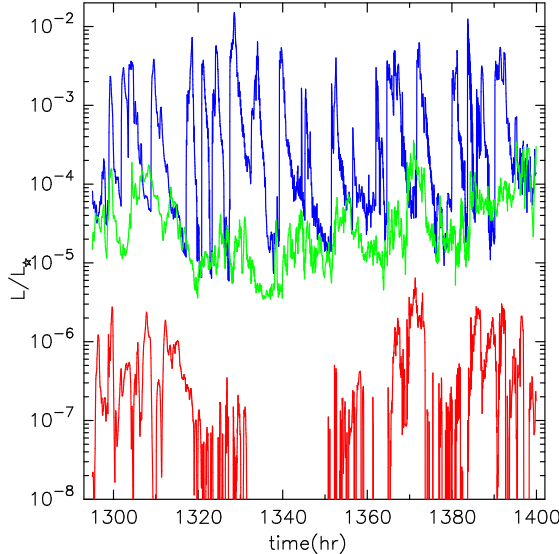


FIG. 21.— The same as Figure 20 but for Model III.

The emission levels of the hot components of the $1 M_{\odot}$ stars are smaller than that of the $3 M_{\odot}$ star. This is because the velocity amplitude of the surface convection is smaller in a less massive star owing to the lower T_{eff} (Equation 9). Interestingly, observations indicate that UV/X-ray emission of RGB stars are positively correlated with stellar mass (Hünsch & Schröder 1996), which might be explained by the difference of the surface amplitudes.

The average emission level of the hot component of Model III is $L_{\text{hot}}/L_{\star} \approx 10^{-6}$ which is marginally smaller than the typical observed X-ray flux ($L_{\text{X}}/L_{\star} = 10^{-7} - 10^{-4}$; e.g. Ayres 2005) from RGB stars blueward of the DL. Moreover, the emissions are from bubbles with $\lesssim 10^6$ (K) in our simulation, which corresponds to EUV rather than soft-X ray emissions. Then, it seems to be difficult to explain the typical X-ray flux by our simulation which only considers the open magnetic field region. It is supposed that closed magnetic loops play a role in the X-ray emission. Hot plasma with $T \gtrsim 10^6$ K can be confined in closed loops by magnetic fields even if the sound speed exceeds the escape velocity. Incidentally, Rosner et al. (1995) speculated that the DL is reflection of the change of magnetic topology; as a star crosses the DL, the magnetic structure becomes open and the hot plasma is liberated to be X-ray deficient.

5. DISCUSSION

5.1. Magnetic Fields

When performing the simulations, we have to set up in advance the surface fluctuations and the magnetic flux tubes. While we can reasonably estimate the amplitude and period (spectrum) of the surface fluctuations from the conditions of the convection zones (§2.3), there are large uncertainties in the properties of the magnetic fields.

We only consider the open magnetic field regions because our aim is to study the stellar winds. We assume the same magnetic field strength ($B_0 = 240$ G) at the surface and expansion factor ($f_{\text{tot}} = 240$) in the

different stars. Although it is unclear how in reality open magnetic flux tubes are, we had better consider effects of different flux tubes for complete discussion (see Falceta-Conçalves, Vidotto, & Janenco-Pereira (2006) for configurations of flux tubes).

We have actually studied effects of the strength and configuration of magnetic flux tubes on the solar wind by both numerical simulations (Suzuki & Inutsuka 2006) and analytical method (Suzuki 2006). We showed that B_0/f_{tot} is a more important parameter which controls the solar wind than individual B_0 and f_{tot} , if the non-linear Alfvén wave dominantly works in the acceleration. For example, flux tubes with different B_0 and f_{tot} but the same ratio B_0/f_{tot} give the similar wind properties if the photospheric amplitudes are the same. The input energy flux is $\sim \rho \langle \delta v_0 \rangle^2 v_{A,0} \propto B_0$ at the surface, and it is diluted according to $1/fr^2$ in the expanding flux tube. The acceleration of the wind mainly occurs in the outer region where the super-radial expansion of the flux tube already finishes. Therefore, B_0/f_{tot} , which is proportional to S_c (≈energy flux) of the input Alfvén wave *measured at the outer region*, becomes the important control parameter in the Alfvén wave-driven wind. Moreover, the mass flux, *i.e.* \dot{M} , is determined almost solely by $\langle \delta v_0 \rangle^2$ at the surface, and very weakly dependent on B_0/f_{tot} (Suzuki & Inutsuka 2006). Then, B_0/f_{tot} plays a role only in tuning the terminal velocity of the solar wind.

This argument is directly applicable to RGB star winds. \dot{M} of the winds (the top panel of Figure 4) are determined with little uncertainty since they are mainly determined by $\langle \delta v_0 \rangle^2$ of the surface convections. However, when we discuss the wind terminal speed, B_0/f_{tot} needs to be taken carefully; wind speed becomes faster in a flux tube with larger B_0/f_{tot} .

$B_0/f_{\text{tot}} (= 240/240 = 1$ G) corresponds to the total magnetic flux over the whole open field regions which is divided by the entire stellar surface. To discuss the average field strength we have to take into account closed regions which occupy a sizable fraction of the surface. If 10% of the surface is occupied by open field regions, the average strength becomes 10 times, namely 10G. This value is quite reasonable from an energetics point of view. The magnetic energy density at the surface becomes $B_0^2/8\pi \simeq 4$ erg cm $^{-3}$, which is considerably smaller than the kinetic energy of the surface turbulence, $\rho \langle \delta v_0 \rangle \sim 10^3 - 10^4$ erg cm $^{-3}$. It is sufficient only if ~ 0.1 % of the turbulent energy is converted to the magnetic energy by motions of charged particles (*i.e.* current) in the surface convection.

Related to this, Rosner et al. (1991, 1995) try to interpret the DL by the change of the magnetic topologies. The stellar rotation becomes slow with the evolution and generation of magnetic fields by large-scale dynamo is switched-off. Magnetic fields are generated by (small-scale) turbulent convection of surface layers in evolved stars. As a result, closed fields, which have dominantly covered the surface in unevolved stars, become open in evolved stars redward of the DL. Therefore, hot plasma, which was well confined by closed loops in less evolved stars, would flow out.

If this scenario is correct, the surface field strength, B_0 , becomes smaller in evolved stars. However, we expect that the field strength in the outer regions, $\propto B_0/f_{\text{tot}}$,

is less affected, because an decrease of B_0 firstly reduces a fraction of closed structures rather than strength of open fields in the outer region ($\propto B_0/f_{\text{tot}}$), before all field lines become open. B_0/f_{tot} is the more important control parameter of the stellar wind than B_0 as stated above. Therefore, we anticipate that our results of the stellar winds are affected little even if the magnetic field topologies change with the stellar evolution.

5.2. Supersonic Transition Locus ?

Before the first report of the DL (Linsky & Haisch 1979), a pioneering concept of a supersonic transition locus (STL) in the HR diagram was introduced to explain the transition from sparse coronal winds of MS stars to dense cool winds of RGB stars (Mullan 1978). As a star expands from MS to RGB, the sonic point, where the wind velocity exceeds the local sound speed, measured in unit of r/R_\star moves inward, and eventually the sound speed becomes larger than the escape velocity even at the base of the corona. Namely, the entire corona becomes supersonic after crossing the STL. This results in the onset of massive stellar wind with larger \dot{M} .

However, our result is not consistent with this view. Our simulations have shown that in the evolved stars the static regions are formed above the photospheres and the sonic points rather move outward even measured in r/R_\star . The winds start to stream out from several R_\star . The densities are still sufficiently high there, which is the main reason why the winds become massive and slow. In the Alfvén wave-driven wind, the rapid increase of \dot{M} is not due to the STL, but due to the large density in the atmosphere.

When discussing the STL, Mullan (1978) assumed isothermal coronae and calculated the temperatures based on the model of the minimum flux stellar coronae (Hearn 1975). The temperature is still high in RGB stars, and $T \simeq 4 \times 10^5$ K on the STL. However, we have shown that this is in the thermally unstable domain and the temperature should become lower, $T \lesssim 10^5$ K. Then, the sound speed becomes smaller, and the coronal base is not supersonic but subsonic.

5.3. Previous Wind Calculations

Hartmann & MacGregor (1980) investigated stellar winds from late-type stars with explicitly taking into account the effects of Alfvén waves. They calculated many models with different stars, wave energies, and wave dissipation parameters under the steady-state condition from assumed inner boundaries. They concluded that the dissipation of Alfvén waves results in coronal heating in higher gravity stars (MS and SG) and mass loss in lower gravity stars (RGB). Our analysis of the time-average wind structures basically confirm this result (§3), whereas our simulations have revealed the various important time-dependent aspects (§4).

Previous works claim that it is difficult to accelerate slow and dense RGB winds by Alfvén waves (Holzer et al. 1983; Charbonneau & MacGregor 1995)². The main problem is that a sizable amount of the input wave energy remains in the supersonic region which

leads to faster wind. The main difference of our results from the previous works is that the large subsonic regions are formed in our simulations due to the nearly static regions above the surfaces. Therefore, most of the input Alfvén wave energies are deposited in the subsonic regions, which results in the slow winds, although the dissipation is not much faster than in the previous model calculations.

We speculate that our wind solutions of the dynamical simulations correspond to “inner solutions” introduced by Holzer et al. (1983). They pointed out that there are two transonic solutions in some cases; one of which is the inner solution in which the wind is accelerated very gradually and the wind speed is slower, although they mainly studied the other one, the outer solution, in which the acceleration starts just above the surface. Our dynamical simulations automatically select stable transonic wind solutions. Then, our results might show that the inner solution is the stable branch in Alfvén wave-drive winds.

5.4. Limitations

Here we discuss processes and effects which need to be studied in more detailed calculations.

5.4.1. Heating of Low Chromosphere: Sound Waves?

We do not input longitudinal fluctuations at the photospheres which would directly drive sound waves, because they do not contribute to the heating and acceleration of the stellar winds (e.g. Judge & Carpenter 1998), whereas sound waves generated from Alfvén waves in the upper regions by the mode conversion in our simulations (§3.6). However, such sound waves directly generated from the surface might be important in the heating of low chromosphere (e.g. Carlsson & Stein 1997). We switch off the radiative cooling in the inner regions if $T < 3000$ K and $\rho > 5 \times 10^{-17}$ g cm⁻³ by the technical reason (§2.2). By taking into account the longitudinal perturbations at the photospheres, we may carry out a more self-consistent treatment of the chromospheres without switching off the radiative cooling artificially.

5.4.2. Multi-dimensional Effects -Wave Generation-

In our simulations we only consider the waves from the photospheres in the 1D flux tubes. However, interactions between flux tubes may be important in generation of waves, though 2D or 3D modeling is required to study such processes. For example, reconnection events between closed loops could be sources of small flare-like events, and these events probably excite compressive waves at locations above the photosphere (Sturrock 1999). In the solar condition, these waves can contribute to the coronal heating since they can avoid attenuation in the chromosphere, unlike those generated from the photosphere which are damped in the chromosphere (Suzuki 2002). In RGB stars, such waves from upper positions also likely contribute to the heating and acceleration of stellar winds.

The magnetic reconnection between a closed loop and an open field line also possibly excites Alfvén waves traveling upwardly (Miyagoshi et al. 2005). These waves would also play a role in the acceleration of RGB winds. Further detailed analysis is required to estimate how such

² Although these works focus on more massive RGB stars than ours, the result will not change if less massive stars are considered.

waves produced by activities involving closed loops are important with respect to the energetics.

5.4.3. Multi-dimensional Effects - Wave Propagation-

We treat the propagation of Alfvén waves in the 1D flux tube. In other words, Alfvén waves are assumed to travel in the same way in neighboring flux tubes. However, if Alfvén speeds are slightly different in neighboring field lines, the waves become out of phase even if they are generated in the same way at the surface. Then, these Alfvén waves dissipate by phase mixing (Heyvaerts & Priest 1983) through resistivity and viscosity.

It is expected that Alfvén waves in stellar winds become more or less turbulent-like. In this case, Alfvénic turbulence cascade to higher frequency in the transverse direction with respect to underlying magnetic fields (Goldreich & Sridhar 1995). Therefore, nature of dissipation of Alfvén waves might be modified in realistic 3D calculations although in our 1D simulations the Alfvén wave dissipate mainly by the decay instability (§3.6).

5.4.4. Collisionless Effects

We assume the MHD approximation, namely a mean free path with respect to the Coulomb collisions,

$$l_{\text{mfp}} = 9.38 \times 10^7 \text{ cm} \frac{(T/10^6 \text{ K})^2}{n/10^8 \text{ cm}^{-3}}, \quad (31)$$

is smaller than a typical scale. Here, we can take the minimum wavelength, $\lambda_{\text{min}} \simeq v_A \tau_{\text{min}}$, of the Alfvén waves in each Model as a typical scale, hence,

$$\lambda_{\text{min}} > l_{\text{mfp}} \quad (32)$$

is the requirement for the MHD condition, otherwise we have to consider collisionless effects of plasma. This condition breaks in $r \gtrsim 2 R_\star$ of the MS star (Model I) and in $\gtrsim 5 R_\star$ of the SB star (Model II), while in the RGB stars (Models III - VI) it holds in the entire simulation regions because the densities are high and the temperatures are low.

In the collisionless regime, compressive (slow/fast MHD) waves suffer transit-time damping (Barnes 1966; Suzuki et al. 2006), one of collisionless damping processes. Then, the dissipation rate of the slow MHD waves which are nonlinearly generated from the Alfvén waves may be changed. This might further modify the mode conversion rate from the Alfvén waves. Then, the dissipation of the Alfvén waves might be indirectly affected in Models I and II.

5.4.5. Partial Ionization

In the RGB atmospheres, the temperatures sometimes become $10^3 - 10^4$ K as shown in the snap-shot results (Figures 12, 18, & 19). In such circumstances, the gas is not fully ionized but partially ionized. The MHD approximation implicitly assumes that the coupling between ions and neutral atoms is sufficient so that the gas can be treated as one fluid. Otherwise, the friction between these two components plays a role in the dissipation of Alfvén waves.

The rate of the ion-neutral collisions is written as

$$t_{in}^{-1} = \frac{m_n}{m_n + m_i} n_n \langle v_{\text{rel}} \sigma_{in} \rangle, \quad (33)$$

where v_{rel} is the ion-neutral relative velocity, σ_{in} is the ion-neutral collisional cross section, $\langle v_{\text{rel}} \sigma_{in} \rangle \approx 1.9 \times 10^{-9} \text{ cm}^3 \text{s}^{-1}$ (Draine, Roberge, & Dalgarno 1983), m_i and m_n are the typical ion and neutral masses, n_n is the neutral number density. Even though an ionization fraction is small (n_n is relatively large), $t_{in} \ll \tau_{\text{min}}^{-1}$ in the entire regions of Models III - VI. This indicates that the coupling is sufficient with respect to the low-frequency waves and we do not have to worry about the effect of weakly ionized gas. However, if high frequency Alfvén waves are generated by turbulent cascade, these waves dissipate by the ion-neutral damping more effectively than in fully-ionized gas (Holzer et al. 1983).

5.4.6. Dust Formation

The temperatures of Models IV and VI intermittently become as low as 1000K (Figures 12 & 19). In such low temperature, dusts will be formed. Radiation pressure on dusts is not efficient in driving winds of RGB stars (Judge & Stencel 1991; Vidotto & Janenco-Pereira 2006), whereas it could be important for asymptotic giant branch stars which have larger radii and luminosities. However, Alfvén waves may dissipate by resonance with dust cyclotron frequencies (Vidotto & Janenco-Pereira 2006), which might also give a correction to the dissipation of the Alfvén waves. To study this effect, we have to carefully consider formation processes of dusts in intermittently existing cool ($T \sim 1000$ K) gas.

6. SUMMARY

We have studied the winds of the intermediate and low mass RGB stars near the DL, by comparing with the coronal winds from the MS and SB stars. These stars all have the surface convective layers, which play a major role in driving the stellar winds as well as the UV/X-ray activities because other mechanisms such as centrifugal force and radiation pressure are insufficient. The surface turbulences excite various types of waves, among which the Alfvén wave travels a longer distance and contribute to not only the atmospheric heating near the surface but the wind acceleration in \gtrsim several R_\star .

We have, for the first time, successfully carried out the time-dependent MHD simulations of the RGB winds in the open magnetic field regions from the photospheres to the sufficiently distant locations ($\approx 25 R_\star$). We inject the fluctuations from the photospheres, of which the amplitudes and spectra are estimated from the properties of the surface convection. We have determined the velocities, densities, and temperatures of the stellar winds in a self-consistent manner by taking into account the radiative cooling and thermal conduction; the propagation and dissipation of the MHD waves are automatically treated, and the subsequent heating and acceleration of the gas are also self-consistently handled by the jump conditions of the MHD shocks, using the nonlinear MHD Godunov-MOCCT algorithm.

When the stars evolve to slightly blueward positions of the DL, the steady hot coronae with temperatures, $T \gtrsim 10^6$ K, disappear. In the atmospheres and winds of the RGB stars magnetized hot bubbles and cool chromospheric gas co-exist. The hot bubbles are created in fast MHD shocks and supported by magnetic pressure. Therefore, the densities of the bubbles can be kept low.

The radiative cooling is reduced to balance with the heating so that the bubbles survive much longer than the cooling timescale.

The RGB star wind is structured with many bubbles and blobs, and the mass loss rate and wind speed show large time-variations. The hot bubbles possibly become sources of EUV and soft X-ray emissions of hybrid stars, whereas the cool chromospheric wind might absorb the emissions. The temperatures of the hot bubbles become lower in more evolved and less massive stars, which is consistent with the trends inferred from the observations of hybrid stars.

The wind velocities also drop to 10-100 km s⁻¹ in the RGB stars, which are much slower than the escape speeds at the stellar surfaces. This is mainly because the static atmospheres are formed above the photospheres and the

stellar winds are practically accelerated from several stellar radii. The terminal velocities are controlled by the escape speeds there, and the slower wind can escape.

The mass loss rate, $\dot{M} \propto \rho v_r R_\star^2$, rapidly increases with the stellar evolution from MS to RGB; \dot{M} of the 1 M_\odot RGB star with $\log g = 1.4$ is $10^{-9} - 10^{-8} M_\odot \text{ yr}^{-1}$ which is 5-6 orders of magnitude larger than \dot{M} of the present Sun ($\log g = 4.4$). However, the increase of \dot{M} is continuous, which is in contrast to the velocity and temperature showing the gaps between the SB and RGB stars. This is because the density in the wind drastically rises during this phase, which compensate the rapid decrease of the wind speed.

We thank Profs. T. Tsuji, H. Shibahashi, H. Ando, T. Watanabe, and S. Inutsuka for many fruitful discussions.

REFERENCES

Anderson, C. S. & Athay, R. G. 1989, ApJ, 336, 1089
 Ayres, T. R. 2005, ApJ, 618, 493
 Ayres, T., Linsky, J. L., Vaiana, G. S., Golub, L., & Rosner, R. 1981, ApJ, 250, 293
 Ayres, T. R., Simon, T., Stern, R. A., Drake, S. A., Wood, B. E., & Brown, A. 1997, ApJ, 496, 428
 Barnes, A. 1966, Phys. Fluid, 9, 1483
 Bohn, H. U. 1984, A&A, 136, 338
 Carlsson, M. & Stein, R. F. 1997, ApJ, 481, 500
 Charbonneau, P. & MacGregor, K. B. 1995, ApJ, 454, 901
 Cunts, M. 1990, ApJ, 353, 255
 de Loore, C. 1970, Ap&SS, 6, 60
 Draine, B. T., Roberge, W. G., & Dalgarno, A. 1983, ApJ, 264, 485
 Dupree, A. K. 1986, ARA&A, 24, 377
 Falceta-Concalves, D., Vidotto, A. A., & Janenco-Pereira, V. 2006, MNRAS, 368, 1145
 Girardi, L., Bressan, A., Bertelli, G., & Chiosi, C. 2000, A&AS, 141, 371
 Goldreich, P. & Sridhar, S. 1995, ApJ, 438, 763 - 775
 Goldstein, M. L. 1978 ApJ, 219, 700 - 704
 Gray, D. F. 1992, "The observation and analysis of stellar photospheres", Cambridge
 Hammer, R. 1982, ApJ, 259, 767
 Hartmann, L., Dupree, A. K., & Raymond, J. C. 1980, ApJ, 236, L143
 Hartmann, L. & MacGregor, K. B. 1980, ApJ, 242, 260
 Hearn, A. g. 1975, A&A, 40, 355
 Heyvaerts, J. & Priest, E. R. 1983, A&A, 117, 220
 Holzer, T., E., Flå, T., & Leer, E. 1983, ApJ, 808
 Holweger, H., Gehlsen, M., & Ruland, F. (1978), A&A, 70, 537
 Hünsch, M. & Schröder, K.-P. 1996, A&A, 309, L51
 Jacques, S. A. 1977, ApJ, 215, 942
 Judge, P. G. & Carpenter, K. G. 1998, ApJ, 494, 828
 Judge, P. G. & Stencel, R. E. 1991, ApJ, 371, 357
 Kim, J. & Ryu, D. 2005, ApJ, 630, L45
 Kopp, R. A. & Holzer, T. E. 1976, Sol. Phys., 49, 43
 Kudoh, T. & Shibata, K. 1999, ApJ, 514, 493
 Landini, M. & Monsignori-Fossi, B. C. 1990, A&AS, 82, 229
 Lamers, H. J. G. L. M. & Cassinelli, J. P. 1999, 'Introduction to Stellar Wind', Cambridge
 Lighthill, M. J. 1952, Proc. Roy. Soc., A211, 564
 Linsky, J. L. & Haisch, B. M. 1979, ApJ, 229, L27
 Miyagoshi, 2005,
 Moore, R. L., Suess, S. T., Musielak, Z. E., & An, A.-H. 1991, ApJ, 378, 347
 Moriyasu, S., Kudoh, T., Yokoyama, T., & Shibata, K. 2004, ApJ, 601, L107
 Mullan, D. J. 1978, ApJ, 226, 151
 Reimers, D. 1975, Mem. Soc. Roy. Sci. Liège, 6e Ser. 8, 368
 Renzini, A., Cacciari, C., Ulmschneider, P., & Schmitz, F. 1977, A&A, 61, 39
 Rosner, R., An, C.-H., Musielak, Z. E., Moore, R. L., & Suess, S. T. 1991, ApJ, 372, L91
 Rosner, R., Musielak, Z. E., Cattaneo, F., Moore, R. L., & Suess, S. T. 1995, ApJ, 442, L25
 Shibahashi, H. 2005, J. Astrophys. Astr. 26, 139
 Stein, R. F. 1967, Sol. Phys. 2, 385
 Stein, R. F., Georgobiani, D., Trampedach, R., Ludwig, H.-G., & Nortlund, Å. 2004, Sol. Phys., 220, 229
 Stencel, R. E. & Mullan, D. J. 1980, ApJ, 238, 221
 Sturrock, P. A. 1999, ApJ, 521, 451 - 459
 Suzuki, T. K. 2002, ApJ, 578, 598
 Suzuki, T. K. 2004, MNRAS, 349, 1227
 Suzuki, T. K. 2006, ApJ, 640, L75
 Suzuki & Inutsuka 2005, ApJ, 632, L49
 Suzuki & Inutsuka 2006, J. Geophys. Res., 111, A6, A06101
 Suzuki, T. K., Yan, H., Lazarian, A., Cassinelli, J. P. 2006, ApJ, 640, 1005
 Terasawa, T., Hoshino, M., Sakai, J. I., & Hada, T. 1986, J. Geophys. Res., 91, 4171
 Tu, C.-Y., Zhou, C., Marsch, E., Xia, L.-D., Zhao, L., Wang, J.-X., & Wilhelm, K. 2005, Science, 308, 519
 Vidotto, A. A. & Janenco-Pereira, V. 2006, ApJ, 639, 416
 Withbroe, G. L. 1988, ApJ, 325, 442
 Yi, S., Demarque, P., & Kim, Y.-C. 1997, ApJ, 482, 677